This article has been accepted for publication in a future issue of this journal, but has not been fully edited. Content may change prior to final publication. Citation information: DOI 10.1109/TAP.2016.2606568, IEEE Transactions on Antennas and Propagation

Sun-Tracking Microwave Radiometry: All-weather Estimation of Atmospheric Path Attenuation at Ka, V and W band

Frank S. Marzano, *Fellow, IEEE*, Vinia Mattioli, *Member IEEE*, Luca Milani, *Member IEEE*, Kevin M. Magde, and George A. Brost

***Abstract*—Sun-tracking microwave radiometry is a ground-based technique where the Sun is used as a beacon source. The atmospheric antenna noise temperature is measured by alternately pointing toward-the-Sun and off-the-Sun according to a beam switching strategy. By properly developing an *ad hoc* processing algorithm, we can estimate the atmospheric path attenuation in all-weather conditions. A theoretical framework is proposed to describe the Sun-tracking radiometric measurements and to evaluate the overall error budget. Two different techniques, based respectively on elevation-scanning Langley method and on surface meteorological data method, are proposed and compared to estimate the clear-air reference. Application to available Sun-tracking radiometric measurements at Ka, V and W band in Rome (NY, USA) is shown and discussed together with the test of new physically-based prediction models for all-weather path attenuation estimation up to about 30 dB at V and W band from multi-channel microwave radiometric data. Results show an appealing potential of this overall approach in order to overcome the difficulties to perform satellite-to-Earth radiopropagation experiments in the unexplored millimeter-wave and submillimeter-wave frequency region, especially where experimental data from a beacon receivers are not available.**

***Index Terms*—Ground-based microwave radiometry, Sun tracking, all-weather path attenuation, clouds and precipitation, microwave and millimeter-wave frequencies.**

I. INTRODUCTION

Atmospheric path attenuation is one of the most important limiting factors for the development of Earth-satellite communications at Ka band and beyond [1], [2]. At these frequencies not only the impact of rain is significantly affecting the channel performances, but also the contribution of atmospheric gases and non-precipitating clouds become non negligible [3], [4]. Radiopropagation beacon campaigns at Ka band and above are essential to experimentally characterize the medium behavior at these frequency bands from both a physical and a statistical point of view (e.g., [5]-[7]). However, these campaigns are conditioned by the limited number of dedicated space missions or by the opportunistic satellite constraints. An alternative way to approach the estimate and the monitoring of path attenuation is to resort to ground-based remote sensing techniques such as weather radar and microwave radiometers (MWR) (e.g., [8],[9]). The first are typically operated at frequencies less than 10 GHz so that a frequency scaling approach is needed for millimeter-wave estimates [10]. The latter are designed up 183 GHz, but they may be inadequate in presence of intense atmospheric scattering [11].

The estimation of atmospheric path attenuation from ground-based microwave radiometers (MWRs) may be affected by a significant underestimation during rain events, especially at frequencies higher than Ku band (e.g., [12],[13]). These errors are mostly due to the use of fixed empirical values or clear-air based estimates of the mean radiative temperature within path-attenuation retrieval algorithms [14], [15]. Model-based approaches have been proposed in the recent literature to overcome this problem by including multiple-scattering effects in the radiative transfer training schemes [16]. Indeed, microwave radiometric measurements of path attenuation during rainy and cloudy conditions can be accomplished in a quite accurate way by exploiting the detection of the solar beacon and a Sun-tracking (ST) operation mode [17]. This approach is quite well known in radioastronomy where it has been used for the estimation of the Sun brightness temperature at microwave and millimeter-wave frequencies (e.g., [18]-[20]). The application of ST in radiopropagation for estimating attenuation during rain was envisaged in early works [21]-[23].

The basic idea of Sun-tracking microwave radiometry (ST-MWR) consists in using the Sun as a source of radiation: the sky microwave emission is measured by alternately pointing toward-the-Sun and off-the-Sun, with and without the Sun contribution in the main lobe, according to a beam switching strategy [17],[23]. Observations toward-the-Sun and off-the-Sun fulfill two main goals: i) under clear-sky conditions they allow to compute the Sun brightness temperature at the different frequencies; ii) during rain events, they allowed to compute the path attenuation due to the rainfall. By properly

Manuscript received September 5, 2016. This work has been partially funded by the EOARD HiRadProp project within the US-AFL EOARD program and by Sapienza University of Rome, Italy.

F. S. Marzano and L. Milani are with the Department of Information Engineering (DIET), Sapienza University of Rome, Via Eudossiana 18, 00184 Rome, Italy, and also with the Center of Excellence CETEMPS, University of L'Aquila, Italy (e-mail: marzano@diet.uniroma1.it; milani@diet.uniroma1.it).

V. Mattioli is with the Center of Excellence CETEMPS, University of L'Aquila, Italy. Currently she is with EUMETSAT, Darmstadt, Germany (e-mail: vinia.mattioli@eumetsat.it)

K.M. Magde and G.A. Brost are Air Force Research Laboratory, Rome, NY, USA (email: kevin.magde@rl.af.mil, george.brost@rl.af.mil)

Color versions of one or more of the figures in this paper are available online at http://ieeexplore.ieee.org.

This article has been accepted for publication in a future issue of this journal, but has not been fully edited. Content may change prior to final publication. Citation information: DOI 10.1109/TAP.2016.2606568, IEEE Transactions on Antennas and Propagation

choosing the switching time interval and taking into account the main lobe aperture, we can infer the atmospheric attenuation along the observed path in all-weather condition through indirect evaluation of the difference between the two measurements [17].

The ST-MWR technique is here thoroughly examined and applied to microwave radiometric measurements at Ka, V and W band [17],[24],[25]. The available dataset consists of measurements, collected in 2015, by a ground-based microwave radiometer with a tracking control stepping motor recently installed in Rome, NY, USA. This new radiometer has four channels with receivers at 23.8, 31.4, 72.5 and 82.5 GHz and is an adaptation of a previous system [26]. The exploitation of ST-MWR in this experiment is aimed at characterizing the millimeter-wave atmospheric channels from V to W band for Geosynchronous Earth-orbit (GEO) and Low Earth-orbit (LEO) satellite communications without resorting to *ad hoc* radiopropagation beacon experiments.

This article is organized as follows. In section II the theoretical foundations of ST-MWR will be reviewed and main assumptions clearly identified. Subsections II.A and II.B will discussed two different techniques to estimate the brightness temperature of the Sun disk, whereas in subsection II.C a sensitivity analysis framework is proposed to examine the predicted performances in terms of errors with respect to antenna pattern, beam filling and Sun brightness temperature uncertainties. Section III is devoted to the description of the available ST-MWR data and to the development of physically-based path-attenuation prediction models in all-weather conditions. In section IV the comparison of ST-MWR estimated atmospheric path attenuations with those obtained from physically-based parametric prediction models at Ka, V and W band is presented. Finally, in section V conclusions and future developments are discussed.

II. Sun-tracking microwave radiometry

For ground-based observations, the out-of-the-Sun (*ooS*) sky brightness temperature T_{BooS}, impinging upon the microwave radiometer antenna along the zenith angle θ and azimuth φ, is given by [27]:

$$T_{BooS}(\theta,\varphi) = T_{mr}(\theta,\varphi)\left[1 - e^{-\tau(\theta,\varphi)}\right] + T_{cos}e^{-\tau(\theta,\varphi)} \quad (1)$$

where τ is the atmospheric optical thickness or path attenuation (in Neper), T_{mr} is the sky mean radiative temperature, and T_{cos} is the brightness temperature of the cosmic background (equal to about 2.73 K). The frequency dependence of parameters is here neglected in favour of geometric considerations. The antenna noise temperature T_{AooS} along the antenna pointing angle (θ_0,φ_0) is the convolution between the sky brightness temperature and the antenna directivity pattern $D(\theta,\phi)$ expressed by [27]:

$$T_{AooS}(\theta_0,\varphi_0) = \frac{1}{4\pi}\int_{4\pi} T_{BooS}(\theta,\varphi)D(\theta_0,\varphi_0,\theta,\varphi)d\Omega \quad (2)$$

When observing the Sun, the toward-the-sun (*twS*) antenna noise temperature T_{AtwS} is due not only to the Sun brightness temperature, but also to the sky brightness temperature emitted by the observed portion within the antenna beamwidth so that:

$$T_{AtwS}(\theta_0,\varphi_0) = \frac{1}{4\pi}\int_{\Omega_{sun}} T_{BtwS}(\theta,\varphi)D(\theta_0,\varphi_0,\theta,\varphi)d\Omega + \frac{1}{4\pi}\int_{\Omega_{sky}} T_{BooS}(\theta,\varphi)D(\theta_0,\varphi_0,\theta,\varphi)d\Omega \quad (3)$$

where $\Omega_{sun} + \Omega_{sky} = 4\pi$ with Ω_{sun} and Ω_{sky} the solid angles subtended by the antenna beam when observing the Sun disk and the sky, respectively and 4π equal to the total solid angle. It holds for the antenna radiation-pattern solid angle Ω_{Pant} (which is basically a solid angle taking into account the antenna radiation intensity normalized pattern):

$$\int_{4\pi} D(\theta,\varphi)/D_M d\Omega = \Omega_{Pant} \quad (4)$$

where D_M is maximum directivity. The *twS* sky brightness temperature is given by

$$T_{BtwS}(\theta,\varphi) = T_{Bsun}e^{-\tau(\theta,\varphi)} + T_{mr}(\theta,\varphi)\left[1 - e^{-\tau(\theta,\varphi)}\right] + T_{cos}e^{-\tau(\theta,\varphi)} \quad (5)$$

where T_{Bsun} is the Sun brightness temperature. If we can approximately consider the brightness temperatures constant within the beam, then (3) can be rewritten as (for simplicity, we neglect here the angle dependence):

$$T_{AtwS} = T_{BtwS}\frac{1}{4\pi}\int_{\Omega_{sun}} D(\theta,\varphi)d\Omega + T_{BooS}\frac{1}{4\pi}\int_{\Omega_{sky}} D(\theta,\varphi)d\Omega = T_{BtwS}\Omega_{Psun} + T_{BooS}\Omega_{Psky} \quad (6)$$

where Ω_{Psun} and Ω_{Psky} are the antenna radiation-pattern solid angles due to Ω_{sun} and Ω_{sky} solid angles. Considering that from (4) it holds $\Omega_{Psky} = \Omega_{Pant} - \Omega_{Psun}$, substituting the brightness temperature expressions (5) into (6) and dividing by Ω_{Pant}, we get:

$$T_{A_{twS}} \cong f_\Omega[T_{Bsun}e^{-\tau} + T_{mr}(1 - e^{-\tau}) + T_{cos}e^{-\tau}] + (1 - f_\Omega)[T_{mr}(1 - e^{-\tau}) + T_{cos}e^{-\tau}] \quad (7)$$

being the beam-filling factor f_Ω the ratio between the (directivity-weighted) Sun radiation solid angle and the antenna beamwidth radiation solid angle (see also (6)), defined as:

$$f_\Omega = \frac{\Omega_{Psun}}{\Omega_{Pant}} = \frac{\Omega_{Pant} - \Omega_{Psky}}{\Omega_{Pant}} \quad (8)$$

By reintroducing the angle dependence, the previous equation for the *twS* mode can be further rewritten as:

$$T_{A_{twS}}(\theta_0,\varphi_0) \cong f_\Omega T_{Bsun}e^{-\tau(\theta_0,\varphi_0)} + T_{mr}(\theta_0,\varphi_0)\left[1 - e^{-\tau(\theta_0,\varphi_0)}\right] + T_{cos}e^{-\tau(\theta_0,\varphi_0)} \quad (9)$$

This article has been accepted for publication in a future issue of this journal, but has not been fully edited. Content may change prior to final publication. Citation information: DOI 10.1109/TAP.2016.2606568, IEEE Transactions on Antennas and Propagation

Analogously, for the *ooS* mode, under the same assumptions, it holds

$$T_{AooS}(\theta_0,\varphi_1) = T_{BooS}(\theta_0,\varphi_1) \cong T_{mr}(\theta_0,\varphi_1)\left[1 - e^{-\tau(\theta_0,\varphi_1)}\right] + T_{cos}e^{-\tau(\theta_0,\varphi_1)} \quad (10)$$

The different azimuth angles φ_0 and φ_1 are due to the ST operational mode. At each elevation θ_0, the azimuth angle is switched from *twS* φ_1 to *ooS* φ_0.

A. Estimation of atmospheric path attenuation

Assuming that the switching between *ooS* and *twS* observation modes is fast enough and the elevation angle θ_0 is kept constant (so that atmospheric attenuation does not change), the Sun-tracking antenna noise temperature difference for each pointing angle can be expressed by:

$$\Delta T_A(\theta_0,\varphi_0,\varphi_1) = T_{AtwS}(\theta_0,\varphi_0) - T_{AooS}(\theta_0,\varphi_1) \quad (11a)$$

Note that the beam-filling factor f_Ω can be dependent from the pointing angle itself. Substituting (9) and (10) into (11a) and assuming the mean radiative temperature and optical thickness do not change between the two observation modes (that is, $T_{mr}(\theta_0,\varphi_0) \cong T_{mr}(\theta_0,\varphi_1)$ and $\tau(\theta_0,\varphi_0) \cong \tau(\theta_0,\varphi_1)$), we get:

$$\Delta T_A(\theta_0,\varphi_0) \cong f_\Omega(\theta_0,\varphi_0)T_{Bsun}e^{-\tau(\theta_0,\varphi_0)} = T^*_{Bsun}e^{-\tau(\theta_0,\varphi_0)} \quad (11b)$$

From (11b), we can estimate the atmospheric optical thickness τ (in Np) in all-weather condition by means of:

$$\hat{\tau}(\theta_0,\varphi_0) = ln\left[\frac{T^*_{Bsun}(\theta_0,\varphi_0)}{\Delta T_A(\theta_0,\varphi_0)}\right] \quad (12a)$$

and in terms of path attenuation *A* (in dB)

$$\hat{A}(\theta_0,\varphi_0) = 4.343\hat{\tau}(\theta_0,\varphi_0) = 4.343ln\left[\frac{T^*_{Bsun}(\theta_0,\varphi_0)}{\Delta T_A(\theta_0,\varphi_0)}\right] \quad (12b)$$

where T^*_{Bsun} is the brightness temperature of the Sun weighted by the beam filling factor f_Ω.

Previous expression shows that path attenuation can be estimated once f_Ω and weighted Sun brightness temperature T^*_{Bsun} are known. The first one can be derived from the antenna pattern and the pointing angle knowledge (with a given resolution and accuracy), whereas the second one must be estimated from the available measurements. Note that the dependence of the beam-filling factor f_Ω on the pointing angle can be neglected if the radiometric system is properly designed and set up; an evaluation of the residual errors will be shown in section II.C.

B. Estimation of Sun brightness temperature

As mentioned, in order to estimate atmospheric path attenuation *A*, the weighted Sun brightness temperature T^*_{Bsun} must be estimated. Two approaches can be foreseen: i) the Langley elevation-based self-consistent method; ii) the Tmr-based meteorologically-oriented method. Both methods assume the availability of radiometric measurements in clear air conditions where a plane-parallel horizontally stratified and azimuthally homogeneous troposphere can be assumed. In these homogeneous conditions we can hypothesize that T^*_{Bsun} estimates are minimally affected by the atmospheric variability. This means that the "*secant law*" can be applied to describe the zenith angle dependence of antenna noise temperatures.

(i) The *Langley technique* starts from (11) which can be rewritten in clear air as (e.g.,[18], [28]):

$$ln[\Delta T_A(\theta_0)] = \ln[f_\Omega T_{Bsun}] + \tau_{clr}(\theta_0) = \ln[T^*_{Bsun}] + \tau_{zclr}(\theta_0)\,sec(\theta_0) \quad (13)$$

where, due to the previous assumptions, the azimuth dependence has been removed, and the following relation holds between the clear-air slant τ_{clr} and zenith τ_{zclr} optical thickness

$$\tau_{clr}(\theta_0) = \tau_{zclr}(\theta_0)sec(\theta_0) = \tau_{zclr}(\theta_0,\varphi_0)m(\theta_0) \quad (14)$$

In (14) $m(\theta_0)$ stands for atmospheric air mass and is equal to $sec(\theta_0)$. By plotting $ln[\Delta T_A(\theta_0)]$ against air mass $m(\theta_0)$ for available Sun-tracking measurements in clear air and approximating the measurements through a linear best-fitting curve:

$$ln[\Delta T_A(\theta_0)] = a + b\,m(\theta_0) \quad (15)$$

we can estimate T^*_{Bsun}, using (11b), from the intercept of the previous line:

$$\begin{cases}\hat{T}^*_{Bsun}(\theta_0) = \exp(a)\\ \hat{\tau}_{zclr}(\theta_0) = -b\end{cases} \quad (16)$$

Once T^*_{Bsun} is estimated during clear-sky, it is then possible to retrieve the atmospheric path attenuation $A(\theta_0,\varphi_0)$ via (12b) in all weather conditions.

(ii) The *meteorological technique* is based on the radiometer equation in clear air, which can be written from (1) as [27]:

$$T_{Aclr}(\theta_0) \cong T_{Bclr}(\theta_0) = T_{mrclr}\left[1 - e^{-\tau_{zclr}(\theta_0)/\sin(\theta_0)}\right] + T_{cos}e^{-\tau_{zclr}(\theta_0)/\sin(\theta_0)} \quad (17)$$

By using radiosounding profile measurements of meteorological variables, we can simulate T_{Aclr} and T_{mrclr}. Indeed, there are modeling evidences that the mean radiating temperature T_{mrclr} can be estimated directly from surface meteorological measurements in clear air (e.g., [29], [30]):

$$\hat{T}_{mrclr} = a_0 + a_1T_s + a_2p_s + a_3RH_s \quad (18)$$

where a_i are the regression coefficients and T_s, p_s, RH_s are the surface temperature, pressure and relative humidity, respectively. This means that in a horizontally-stratified clear

This article has been accepted for publication in a future issue of this journal, but has not been fully edited. Content may change prior to final publication. Citation information: DOI 10.1109/TAP.2016.2606568, IEEE Transactions on Antennas and Propagation

air we can obtain the zenith atmospheric optical thickness $\tau_{zclr}(\theta_0)$:

$$\hat{\tau}_{zclr}(\theta_0) = \sin(\theta_0) \ln\left[\frac{\hat{T}_{mrclr} - T_{cos}}{\hat{T}_{mrclr} - T_{Aclr}(\theta_0)}\right] \quad (19)$$

From (13), using the Sun-tracking measurements, we can estimate the weighted Sun brightness temperature:

$$ln[\Delta T_A(\theta_0)] = \ln[f_\Omega T_{Bsun}] + \hat{\tau}_{clr}(\theta_0) = \ln[T^*_{Bsun}] + \hat{\tau}_{zclr}(\theta_0)/\sin(\theta_0) \quad (20)$$

that is

$$\begin{cases} \ln[\hat{T}^*_{Bsun}] = \ln[\Delta T_A(\theta_0)] - \hat{\tau}_{zclr}(\theta_0)/\sin(\theta_0) \\ \hat{T}_{Bsun} = \frac{\hat{T}^*_{Bsun}}{f_\Omega} \end{cases} \quad (21)$$

Note that, with respect to the Langley technique, the meteorological technique provides a time series of $\hat{T}^*_{Bsun}$ on a clear-air daily basis. The retrieval of the atmospheric path attenuation $A(\theta_0, \varphi_0)$ via (12) is then performed by taking the mean value of $\hat{T}^*_{Bsun}$ time series.

C. Theoretical error sensitivity analysis

The sensitivity analysis of atmospheric path attenuation estimate to residual errors or uncertainties of ST-MWR measurements is fundamental to understand the expected accuracy of the technique. Several sources of uncertainty can be identified intrinsic in the different techniques (Langley vs meteorological). In order to perform this error budget analysis, we can use for simplicity the first-order error propagation theory by assuming a statistical independence among the error sources.

Path attenuation is directly affected by antenna noise temperature difference uncertainties. The path attenuation error $\delta\tau$ or δA (in dB) with respect to the antenna noise difference uncertainty $\delta\Delta T_A$ is obtained from the governing equation in (12) of ST-MWR leading to:

$$\delta A = 4.343\delta\tau = -\frac{4.343}{\Delta T_A}\,\delta\Delta T_A \quad (22a)$$

Fig. 1a shows the previous equation of δA for ΔT_A values expected in clear sky between those at Ka and W band (see also sect. III.A). As ΔT_A is typically much smaller at Ka band with respect to V band, lower frequencies are more affected by uncertainties in ΔT_A (due to calibration errors, antenna mispointing during Sun tracking and atmospheric variability) with respect to higher frequencies. For an uncertainty in ΔT_A of 6 K, the error in path attenuation goes from -0.05 dB at 82.5 GHz up to -0.27 dB at 23.8 GHz.

Fig. 1b shows the same analysis, but for ΔT_A values expected in rainy situations. Due to the strong attenuation of Sun emission by rain layers, ΔT_A differences are expected to be much smaller than those in clear sky. For heavy rain ΔT_A tends to zero in principle. Although the sensitivity increases for lower ΔT_A values, possible errors associated to antenna mispointing of the Sun position are less important. Nevertheless the atmospheric variability, due to the different observation geometry, is somehow larger.

The sensitivity of δA with respect to uncertainties δT^*_{Bsun} in the estimate of T_{Bsun} is given by

$$\delta A = 4.343\delta\tau = \frac{4.343}{T^*_{Bsun}}\,\delta T^*_{Bsun} \quad (22b)$$

Fig. 1c shows δA for a set of T^*_{Bsun} values which are those expected at K and V band (see sect. III). Alike Fig. 1a, lower frequencies are associated to smaller T^*_{Bsun} values, and are more sensitive to errors in path attenuation. For an uncertainty of T^*_{Bsun} up to 10 K, the error in path attenuation goes from 0.06 up to 0.36 dB; for larger uncertainties, the error can reach 1 dB in Fig. 1c.

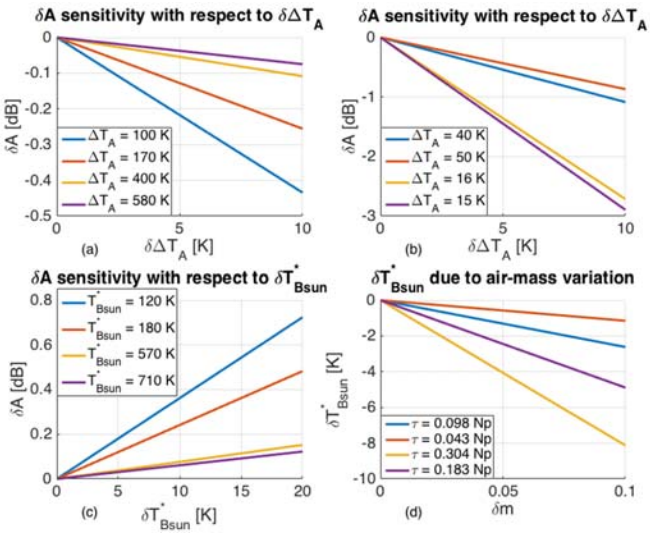

Fig. 1. Sensitivity analysis of ST-MWR performances for typical values, which are those expected between Ka and W band. Blue line corresponds to 23.8 GHz, red line to 31.4 GHz, yellow line to 72.5 GHz and finally violet line to 82.5 GHz. See text for details.

Note that, when using the antenna noise temperature difference, we have assumed the same elevation both of-the-Sun and toward-the-Sun observations. If this is not the case, a further error should be considered. This means that, assuming the out-of-the-Sun observation in (10) is performed at an elevation angle θ_1, the antenna noise temperature difference in (11) should be replaced by:

$$\Delta T_A(\theta_0, \varphi_0, \theta_1, \varphi_1) = T_{AtwS}(\theta_0, \varphi_0) - T_{AoOS}(\theta_1, \varphi_1) \quad (23)$$

By substituting the expressions (9) and (10) into (23) and truncating to the first order the Taylor expansion of the atmospheric transmittance ratio, we can obtain the following T^*_{Bsun} uncertainty due to the air mass variation δm between the two observations:

$$\delta T^*_{Bsun} = (T_{cos} - T_{mr})\tau_{zclr}\,\delta m \quad (24a)$$

Fig. 1d shows the previous equation for a set of τ_z values, which are those expected in clear air between Ka and W band,

This article has been accepted for publication in a future issue of this journal, but has not been fully edited. Content may change prior to final publication. Citation information: DOI 10.1109/TAP.2016.2606568, IEEE Transactions on Antennas and Propagation

and for a fixed mean radiative temperature ($T_{mr} = 270\ K$). For an air-mass uncertainty of about 0.03, corresponding to 0.2 deg at 20 deg elevation, the error in estimating T^*_{Bsun} goes from -0.3 up to -2.5 K, depending on the value of the considered clear air optical thickness (higher τ_{zclr} values give higher errors).

Finally, since ΔT_A values may reach zero or even negative values for heavy rain (when the Sun disk contribution is completely attenuated by the atmosphere), there should be an upper limit of the attainable path attenuation during rain. Starting from (12b), the maximum path atmospheric attenuation value A_{max} depends on both T^*_{Bsun} at the considered frequency and minimum detectable $\Delta T_{A\,min}$ so that:

$$A_{max}(\theta_0, \varphi_0) = 4.343 ln\left[\frac{T^*_{Bsun}(\theta_0,\varphi_0)}{\Delta T_{A\,min}(\theta_0,\varphi_0)}\right] \tag{24b}$$

For typical ΔT_{Amin} values of about 0.5 K (1 K) and T^*_{Bsun} at Ka, V, and W band similar to those in Fig. 1c, the maximum attainable attenuation with the ST-MWR method is about 24-26 dB (21-23 dB) at Ka band and about 31-32 dB (28-29 dB) at V-W band.

III. Available Data and Model-Based Prediction

This section, organized in 2 subsections, is devoted to the description of the available ST-MWR data and to the development of physically-based prediction models at Ka, V and W band to be tested by using ST-MWR measurements.

A. *Experimental setup and MWR data processing*

The available dataset consists of measurements collected by the ground-based Air Force Research Laboratory (AFRL) MWR during May 2015 (20 days) and June 2015 (26 days) in Rome, NY, USA (43.2°N, 75.4° W). The AFRL-MWR has four channels with receivers at 23.8, 31.4, 72.5 and 82.5 GHz and is a modified version of the RPG LPW-U72-82 water-vapor and cloud-liquid microwave radiometer series in order to allow an automatic Sun-switching operation mode [26]. The antenna is shaped to reduce sidelobes (-30dB at K-band and -40 dB at V-,W-band); and the antenna radiation pattern is considered approximately Gaussian with a half-power beamwidth decreasing with the frequency and equal to 3.74°, 2.97°, 1.47°, and 1.30°, respectively. Measurements have been collected at elevation angle between 20° and 70°, with a scan step of 0.1° in both elevation and azimuth, during clear sky days and during raining events.

The processing and quality-control procedures applied to the AFRL-MWR data are described in the following paragraphs.

1) *Clear-air data discrimination.*

For selecting clear-sky days in order to estimate T^*_{Bsun} with both Langley and Meteorological techniques, we have implemented an atmospheric index, a scalar quantity named Status Sky Indicator (SSI), purely based on the available radiometric measurements and successfully applied in several MWR campaigns [30][31]. SSI is defined as:

$$\mathrm{SSI} = \frac{T_{B(31.4\,GHz)} - c}{T_{B(23.8\,GHz)}} \tag{25}$$

where c is a parameter dependent on the atmospheric air mass m, equal to $sec(\theta_0)$. If SSI is minor than a given threshold SSI_{th}, a clear air condition is assumed. In this work and for the Rome, NY, site, we have set $c = -0.13 \cdot m^2 + 6.3 \cdot m + 2.1$ and the $SSI_{th} = -0.00012 \cdot m^2 + 0.0066 \cdot m + 0.31$.

SSI parameterization has been set up by performing radiative transfer simulations at several elevation angles applied to a long-term available radiosonde observation (RaOb) dataset. The closest RaOb site to Rome, NY, is located at Albany County Airport, NY, USA (WMO station ID code 72518, WBAN ID code 14735). RaOb data belonging to the period 1994-2012 have been collected for this study. Downwelling brightness temperatures have been generated using a plane parallel radiative transfer scheme with an updated version of for gas absorption and cloud model [32]-[34].

2) *Filtering toward-the-Sun observations in clear air in the estimation of T^*_{Bsun}.*

In order to estimate T^*_{Bsun} with the Langley technique (see sect. IV.A), the data processing has been designed to select the maximum $T_{A_{twS}}$ for each elevation angle. The AFRL-MWR operational mode maintains a constant elevation for a finite time so that the Sun can move inside the antenna beam during that period. As noted from Fig. 1a, small pointing errors of the Sun position can lead to errors in ΔT_A of several kelvins with a large impact on attenuation estimates, especially at Ka band. The maximum value of $T_{A_{twS}}$ ensures to identify the best matching observation where the Sun disk is centred with respect to the antenna beamwidth.

Finally, a binning average with respect to air mass m has been performed considering steps of 0.2. In this way, an equal distribution of samples in terms of air mass is achieved and the results of the linear regression in (15) are not influenced by the different distribution of samples with airmass.

3) *Antenna noise temperature self-consistency check*

For estimating path attenuation, ST-MWR approach needs valid antenna noise temperature differences ΔT_A between *twS* and *ooS* modes to work properly. These differences may reach zero or even negative during intense rain events, which limits the application of ST-MWR, as discussed in Sect. II.C. In (24b) we have taken into account only differences $\Delta T_{A\,min}$, greater than the MWR brightness temperature absolute accuracy. The latter have been set to 0.5 K at 23-31 GHz and 1 K at 72-82 GHz in agreement with the manufacturer specifications.

ST-MWR measurements are interesting to analyze with respect to their temporal trend. As an example here discussed, **Fig. 2** shows the time series of ST-MWR measurements in terms of *ooS* (lower curves) and *twS* (upper curves) antenna noise temperatures for two case studies referring to a clear air (8 May 2015) and cloudy day (28 May 2015) and for the four AFRL-MWR available frequencies (Fig. 2a-d). **Fig. 3** shows the same as in Fig. 2, but for two different case studies referring to a moderate rain (11 May 2015) and intense rain event (30 June 2015).

This article has been accepted for publication in a future issue of this journal, but has not been fully edited. Content may change prior to final publication. Citation information: DOI 10.1109/TAP.2016.2606568, IEEE Transactions on Antennas and Propagation

As noted in Fig. 2a-b, the behavior of the *ooS* and *twS* antenna temperatures at 23.8 and 31.4 GHz in clear sky is similar with respect to the elevation, being higher values observed at low elevation (at the beginning of the daily Sun-tracking) and reaching minimum values at the solar noon (at the maximum tracking elevation). Conversely, at 72.5 and 82.5 GHz, the behavior of $T_{A_{ooS}}$ and $T_{A_{twS}}$ time series is the opposite, with *twS* time series reaching their maximum values at the solar noon (Fig. 2c and Fig. 2d). Such behavior is explained by recalling (9) and (10) and the different impact of T^*_{Bsun} at Ka and V, W band (see Fig. 1c).

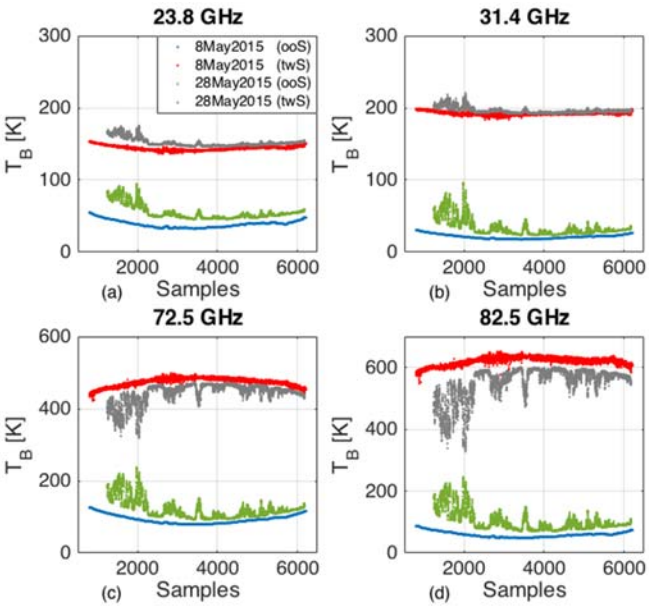

Fig. 2. Time series of ST-MWR measurements in terms of *ooS* (lower couple of curves) and *twS* (upper couple of curves) antenna noise temperatures for two case studies referring to a clear air (8 May 2015, blue dots for *ooS* and red dots for *twS*) and cloudy day (28 May 2015, green dots for *ooS* and grey dots for *twS*) and for the AFRL-MWR available frequencies a) 23.8 GHz; b) 31.4 GHz; c) 72.5 GHz; d) 82.5 GHz.

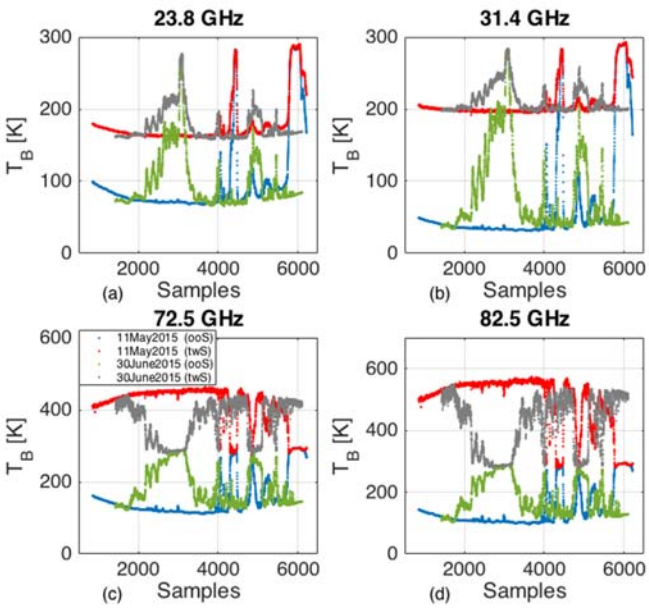

Fig. 3. Time series of ST-MWR measurements as in Fig. 2, but for two case studies referring to a moderate rain (11 May 2015, blue dots for *ooS* and red dots for *twS*) and intense rain event (30 June 2015, green dots for *ooS* and grey dots for *twS*) for the four AFRL-MWR available frequencies a)-d).

At Ka band the atmospheric contribution with airmass still dominates over the one due to the Sun, whereas a V and W band it is the reverse. In presence of clouds, the antenna noise difference between the two measurement modes *ooS* and *twS* decreases when the optical thickness increases (i.e., for each frequency, lower curves tend to to be closer to the upper curves in Fig. 2). This is especially evident in the rainy event where the difference goes to zero as atmospheric extinction significantly increases during rainfall (see Fig. 1b for average ΔT_A values during rainy conditions). As expected, this behavior is more dominant at V and W band than at Ka band.

B. Physically-based prediction models of path attenuation

The ST-MWR technique can offer a very interesting framework to validate parametric prediction models at frequency bands above Ka band where satellite-to-Earth beacon measurements are rare. In previous works physically-based prediction models (PPM) have been proposed for estimating specific atmospheric parameters (i.e. attenuation A, T_{mr} and T_B) as a function of selected input parameters depending on both the frequency and the elevation angle [9], [16]. These models have been based on the non-linear regression fit of numerical simulations, derived from the sky-noise Eddington radiative-transfer model (SNEM) in an absorbing and scattering medium such as gaseous, cloudy and rainy atmosphere [14], [32].

The PPM approach is based on the exploitation of RaOb datasets, collected in a location close to the site of interest and used to statistically characterize the local meteorology in terms of temperature, pressure and humidity average and standard-deviation profiles [24]. The latter statistics is then imposed in the Monte Carlo pseudo-random generation of vertical cloud structures where average profiles and cross-correlation among hydrometeor concentration are imposed [14]. The considered hydrometeor categories are cloud droplets, raindrops, graupel particles, ice crystals and snow aggregates, whereas 9 classes of cloud structures (including nimbostrati and cumulonimbi) are included [16].

The PPM general approach has been adapted for Rome (NY, USA) using our available radiosonde dataset from the site of Albany, NY, USA, about 70 km far away. By extracting the meteorological statistics, SNEM simulations have been performed at 23.8, 31.4, 72.5 and 82.5 GHz and for 8 elevation angles between 20° and 90° in order to compute both brightness temperature and path attenuation.

Fig. 4 (a-d) shows the scatterplot of T_{BooS} versus corresponding path attenuation A at zenith (elevation angle of 90°) for each considered frequency in all weather condition (all cloud classes plus clear air condition). **Fig. 5** (a-d) shows the same as in **Fig. 4**, but for an elevation angle of 36°. Previous scatterplots suggest that a PPM can be developed to estimate path attenuation A from measured antenna noise temperature (in our case T_{BooS}). Two parametric non-linear models are here proposed to estimate path attenuation at 23.8, 31.4, 72.5 and 82.5 GHz using a multifrequency or a dual-

This article has been accepted for publication in a future issue of this journal, but has not been fully edited. Content may change prior to final publication. Citation information: DOI 10.1109/TAP.2016.2606568, IEEE Transactions on Antennas and Propagation

frequency MWR.

The first PPM model is a multi-frequency approach and it is based on a polynomial regression (*Pol*) on SNEM dataset [24], [25]. The proposed multifrequency PPM-*Pol* form is given by:

$$A_{Pol}(f) = m \cdot \sum_{i=1}^{4} a_i \, T_{BooS}(f_i) + \, b_i \, T_{BooS}^2(f_i) \qquad (26)$$

where $f_{i=1,2,3,4}$=23.8,31.4,72.5,82.5 GHz and f is one of 4 available frequencies f_i, whereas the coefficients are all function of the air mass m. **Table A1** in the Appendix provides their expressions and numerical values.

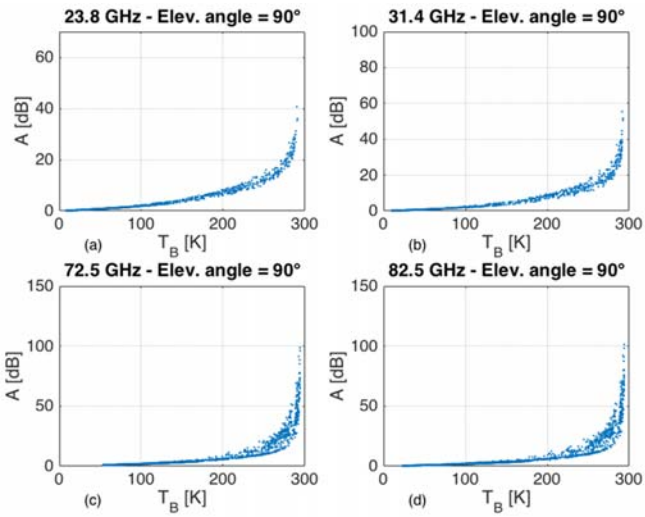

Fig. 4. Scatterplot of T_{BooS} versus corresponding path attenuation A at zenith (elevation angle of 90°) in all weather conditions for each considered frequency a) 23.8 GHz; b) 31.4 GHz; c) 72.5 GHz; d) 82.5 GHz.

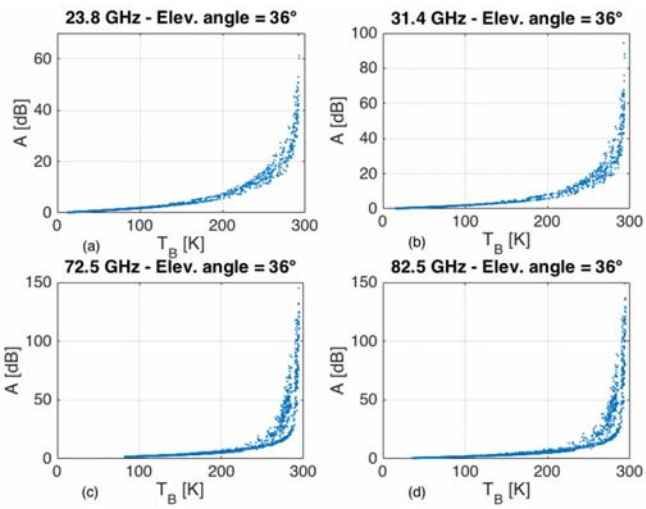

Fig. 5. The same as in Fig. 4, but for an elevation angle of 36°.

The second model (*PolDEx*) is an extended version of PPM-*Pol* approach, reinforced with a double exponential single-frequency term, able to achieve better results in heavier rainy cases. The polynomial and the exponential terms are weighted by the SSI index and tuned through the parameter h. The PPM-*PolDEx* is able, substantially, to balance heavy weather conditions by the double exponential expression with the good results of PPM-*Pol* in cloudy and moderately rainy conditions. The multifrequency PPM-*PolDEx* expression is expressed by:

$$A_{PolDEx}(f) = m\{(1 - SSI + h)A_{Pol}(f) + (SSI - h)A_{DEx}(f)\} \qquad (27a)$$

being the single-frequency double-exponential form given by

$$A_{DEx}(f) = \left[c_1 \cdot \mathrm{e}^{c_2 \cdot T_{BooS}(f)} + d_1 \cdot \mathrm{e}^{d_2 \cdot T_{BooS}(f)}\right] \qquad (27b)$$

where, as in (28), the coefficients a_i and b_i have the same expressions reported in Table A1. The coefficients h, c_1, c_2, d_1 and d_2 are all function of the air mass m. **Table A2** in the Appendix provides their expressions and numerical values.

To highlight the advantages of our all-weather models, we can also show the comparison with the conventional technique using the clear-air approximation of the mean radiative temperature T_{mr} at the frequency f of interest:

$$\hat{A}_{clr}(f) = 4.343 ln\left[\frac{\hat{T}_{mrclr}(f) - T_{cos}}{\hat{T}_{mrclr}(f) - T_{AooSclr}(\theta_0)}\right] \qquad (28)$$

where T_{mrclr} is the clear-air mean radiative temperature estimated by (18). We can expect a significant error when trying to apply (28), instead of (26) or (27), in cloudy and, more importantly, rainy conditions. Note that the difference $\hat{T}_{mrclr}(f) - T_{AooSclr}(\theta_0)$ is less than zero, the estimator in (28) is not applicable. As mentioned, we have conservatively set this applicability limit not to zero, but to 0.5 K for 23 and 31 GHz to 1 K for 72.5 and 82.5 GHz.

In order to evaluate the accuracy of *Pol* and *PolDEx* PPM prediction models, we can evaluate the error of the regressive parametric estimates with respect to corresponding SNEM simulations. **Table A3** in the Appendix shows the intercomparison between *Pol* and *PolDEx* models in terms of root-mean-square-error (RMSE) and average error (AvE), where the error is defined as the difference between the considered model and the simulation. We can clearly note from Table III how the *PolDEx* parametric model shows better results at all frequencies and for all elevation angles. RMSE and AvE values increase with the decrease of the elevation angle, and this behavior is expected as optical thickness (and path attenuation) increases with the decrease of the elevation angle thus meaning that the percentage error is still comparable at any angle.

In order to stress the latter consideration, an index of agreement (IA) has been also considered to better evaluate the percentage accuracy [35]. IA is a standardized measure of the degree of model prediction error and it varies between 0 and 1. An agreement index score of 0 suggests no agreement between the PPM model and the SNEM dataset, while an agreement score of 1 suggests complete match between the model and the dataset. IA is defined as [35]:

$$IA = 1 - \frac{\langle (x_{PPM} - x_{SNEM})^2 \rangle}{\langle (|x_{PPM} - \langle x_{SNEM} \rangle| + |x_{SNEM} - \langle x_{SNEM} \rangle|)^2 \rangle} \qquad (29)$$

where x_{PPM} and x_{SNEM} are the PPM estimate and SNEM reference simulation. Considering the *PolDEx* model at zenith (elevation angle of 90°) in Table III, we can note as IA is

This article has been accepted for publication in a future issue of this journal, but has not been fully edited. Content may change prior to final publication. Citation information: DOI 10.1109/TAP.2016.2606568, IEEE Transactions on Antennas and Propagation

equal to about 0.99 at 23.8 GHz and about 0.84 at 82.5 GHz. The accuracy decreases with the decrease of elevation angle but the IA is always greater than 0.7, that is PPM-*PolDEx* is able to provide reliable results with respect to SNEM dataset.

Worldwide distribution of MWR with channels in V and W bands is still very limited. For this reason a further dual-frequency polynomial model has been developed in order to provide a stand-alone solution only using channels at Ka band, i.e. at 23.8 and 31.4 GHz (e.g., [6]). Indeed, in order to retrieve path attenuation estimate for a dual-channel MWR we might use the double-exponential *DEx* model in (27b) since it is single-frequency and *SSI* exclusively depends on the brightness temperatures at 23.8 and 31.4 GHz. However, an extension to a dual-frequency frequency can improve the results. The dual-frequency PPM-*Pol2* model is given by:

$$A_{Pol2}(f) = m \cdot \sum_{i=1}^{2} a_i \, T_{BoOS}(f_i) + \, b_i \, T_{BoOS}^2(f_i) \qquad (30)$$

where $f_{i=1,2}$=23.8,31.4 GHz and the coefficients are all function of the air mass *m*. **Table A4** in the Appendix provides their expressions and numerical values. Properly replacing $A_{Pol}(f)$ in (27) by $A_{Pol2}(f)$ given by (30), the *PolDEx* model can be used to retrieve path attenuation in all-weather conditions from the MWR measurements at 23.8 and 31.4 GHz only.

IV. Application to Sun-Tracking Data

This section is devoted to the description of results obtained from ST-MWR in terms of path attenuation estimates at Ka, V and W band. This work has been performed according to the following steps: i) careful selection of clear-sky days with minimum atmospheric variability; ii) computation of T_{Bsun}^* by means of both Langley and meteorological methods; iii) application of the Sun-tracking technique to estimate total atmospheric attenuation in all weather conditions with a focus on rainy cases; iv) application of PPM *Pol* and *PolDEx* prediction methods to estimate all-weather total attenuation from *ooS* observations; v) inter-comparison analysis of the retrieved attenuations from steps iii) and iv). Verification of PPM *Pol* and *PolDEx* prediction algorithms is also discussed together with an error budget analysis.

A. Results for Sun brightness temperature estimate

By using the antenna noise temperature difference versus air mass, **Fig. 6** (a-d) shows the estimate of T_{Bsun}^* using the Langley technique, as discussed in sect. II.B, for each frequency and two selected clear-air days (May 8 and May 21, 2015). The best-fitting line is also shown.

Data processing steps for clear-sky, as described in III.A, have been performed to obtain robust estimates of T_{Bsun}^* in order to ensure as much as possible a constant daily optical thickness. For the Langley technique, this means to obtain a linear dependence with a relatively small deviation in (15), being τ_{zclr} the slope in the linear approximation.

By using the times series of antenna noise temperature difference, **Fig. 7** (a-d) shows the estimate of T_{Bsun}^* using the meteorological technique for each frequency and the two selected clear-air days. The average value of T_{Bsun}^* is also highlighted as a constant line. The regression coefficients a_0, a_1, a_2 and a_3, used to estimate T_{mrclr} in (18), are reported in **Table I** for completeness.

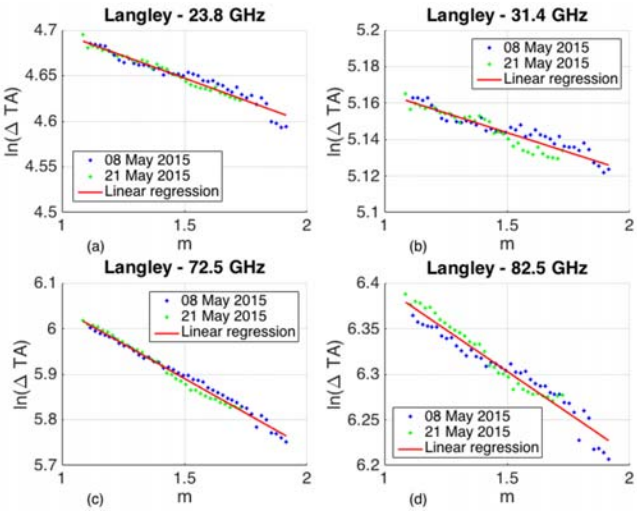

Fig. 6. Estimate of T_{Bsun}^* using the Langley technique, as discussed in sect. II.B, for each frequency and the 2 selected clear-air days.

TABLE I. Mean radiative temperature regression coefficients for applying the meteorological technique

f [GHz]	a_0 [K]	a_1 [K/K]	a_2 [K/mbar]	a_3 [K/%]
23.8	-118.65	0.962	0.107	0.146
31.4	-125.65	0.99	0.102	0.162
72.5	-110.88	0.932	0.102	0.155
82.5	-134.49	1.03	0.099	0.170

In terms of Sun emission variation at the involved frequencies, we have assumed that the long-term component is small, also considering that the antenna beamwidth is much larger than the Sun arch. Indeed, we have not observed noticeable variations of the estimated Sun brightness temperature in our measurements, even though this should be proved on a longer dataset.

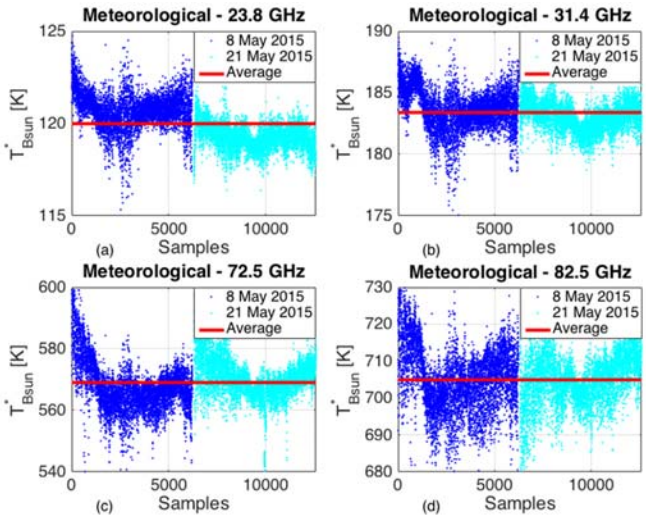

Fig. 7. Estimate of T_{Bsun}^* using the meteorological technique for the two

This article has been accepted for publication in a future issue of this journal, but has not been fully edited. Content may change prior to final publication. Citation information: DOI 10.1109/TAP.2016.2606568, IEEE Transactions on Antennas and Propagation

selected clear-sky days (May 8, blue dots; May 21 cyan dots) at each frequency a) 23.8 GHz; b) 31.4 GHz; c) 72.5 GHz; d) 82.5 GHz.

Table II shows the intercomparison between the Langley and meteorological technique estimates for T^*_{Bsun} together with the confidence intervals (in terms of standard deviation for the meteorological technique and the maximum deviation for the Langley technique). Note that Table I also provides the values of τ_{zclr} and the maximum deviations $\sigma_{\tau_{zclr}}$ (which is below 5% at all frequencies thus proving a good selection of clear-sky days). The uncertainty of T^*_{Bsun} estimates is comparable for both Langley and meteorological techniques, even though small differences are noted above Ka band.

TABLE II. INTERCOMPARISON OF LANGLEY AND METEOROLOGICAL ESTIMATES OF WEIGHTED SUN BRIGHTNESS TEMPERATURE

	Langley				Meteorological	
f [GHz]	T^*_{Bsun}[K]	$\sigma_{T^*_{Bsun}}$[K]	τ_{zclr}[Np]	$\sigma_{\tau_{zclr}}$[Np]	T^*_{Bsun}[K]	$\sigma_{T^*_{Bsun}}$[K]
23.8	120.82	0.96	0.098	0.005	119.99	1.11
31.4	182.78	1.03	0.043	0.004	183.40	1.47
72.5	570.56	7.19	0.304	0.008	569.07	7.49
82.5	719.22	10.90	0.183	0.010	704.92	8.12

B. *Results for path attenuation estimate*

The ST-MWR technique is intrinsically based on a variable antenna pointing in order to follow the Sun movement along its ecliptic. In order to make atmospheric path attenuation values intercomparable, we can show all results in terms of the zenith-equivalent path attenuation, obtained by multiplying each estimated path attenuation for the corresponding air mass. Note that from (24b), setting $\Delta T_{A\,min}$ to 0.5 K (Ka band) and 1 K (V-W band) and using T^*_{Bsun} Langley-based results reported in Table II, the upper limit A_{max} is equal to 23.83 dB, 25.63 dB, 27.56 dB and 28.57 dB, at 23.8, 31.4, 72.5 and 82.5 GHz, respectively.

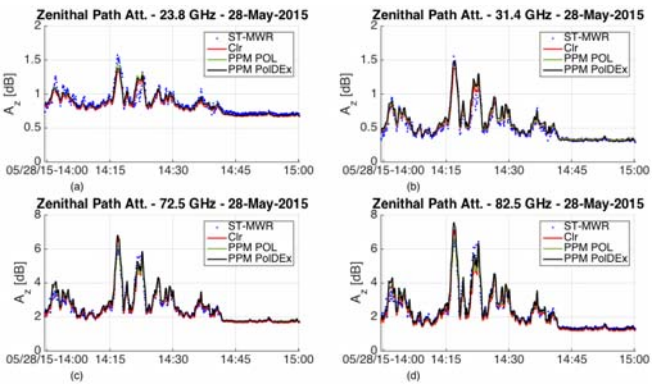

Fig. 8. Time series of zenith-equivalent path attenuation estimates on May 28, 2015 (cloudy case) at a) 23.8 GHz; b) 31.4 GHz; c) 72.5 GHz; and d) 82.5 GHz-

As an example, **Fig. 8** (a-d) shows the time series of zenith-equivalent attenuation estimates at 23.8, 31.4, 72.5 and 82.5 GHz respectively, for the cloudy case of Fig. 2. Predictions, based on models from PPM *Pol* in (26), PPM *PolDEx* in (27), and *Clr* in (28), are compared against ST-MWR attenuation retrievals. All parametric prediction models, as expected in this case, provide quite good results in agreement with ST-MWR time series.

Fig. 9 (a-d) shows a time series similar to Fig. 8, but for the intense rainy event of Fig.3. Especially at 72.5 and 82.5 GHz, as expected, the application of the *Clr* model is not adequate to retrieve path attenuation during rain.

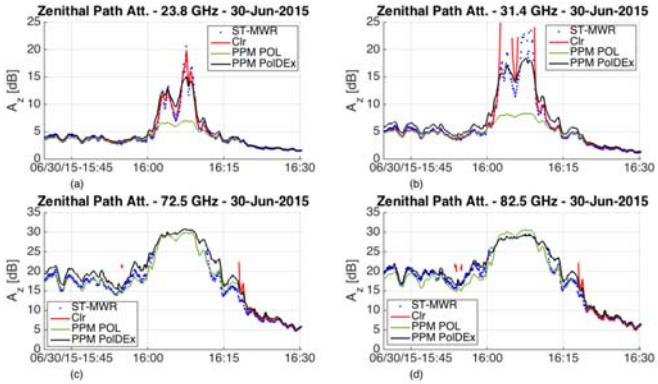

Fig. 9. Time series of zenith-equivalent path attenuation estimates on June 30, 2015 (rainy event) at a) 23.8 GHz; b) 31.4 GHz; c) 72.5 GHz; and d) 82.5 GHz.

For an overall quantitative estimation of the PPM prediction approaches, **Fig. 10** (a-d) shows the scatterplot of *PolDEx* and *Clr* model estimates for each frequency versus the corresponding ST-MWR *A* for all weather conditions and the all available dataset. **Fig. 11** (4x4) shows the same comparison as in Fig. 10, but for *Pol* model. **Table III** quantifies the comparison in terms of RMSE and AvE, where the error is defined as the difference between prediction model under consideration and ST-MWR.

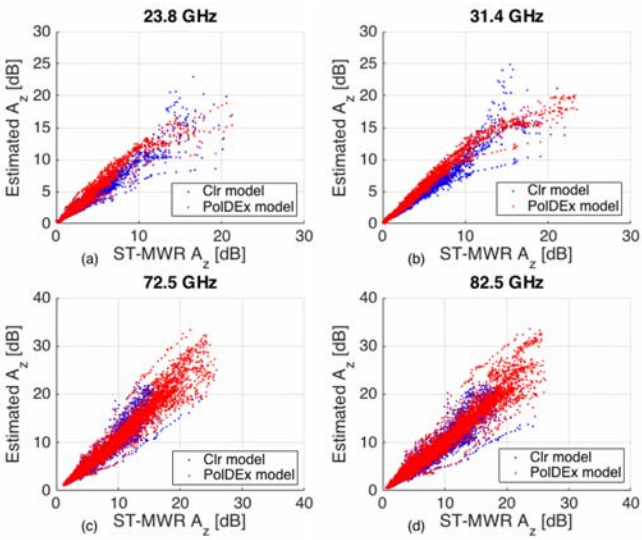

Fig. 10. Scatterplot of ST-MWR path attenuation for each frequency versus path attenuation estimated from PolDEx and Clr models for all weather condition.

From Fig. 10 and 11 it is worth noting that the PPM *Pol* prediction tends to underestimate significantly path attenuation at Ka band, showing performances even worse than *Clr* prediction. On the other hand, the *PolDEx* approach shows a fairly good correlation with reference ST-MWR data

This article has been accepted for publication in a future issue of this journal, but has not been fully edited. Content may change prior to final publication. Citation information: DOI 10.1109/TAP.2016.2606568, IEEE Transactions on Antennas and Propagation

for all frequencies, whereas the *Clr* model is much worse than the other models at V and W band. Note that the latter is not even applicable in rainy conditions and at higher frequencies when the atmosphere is opaque. Table III confirms these visual considerations stressing the very low bias of PolDEx estimates and its flexibility in dealing with both clear and rainy cases. Note that the scores of the Clr model are slightly optimistic as they computed for a reduced number of applicable points.

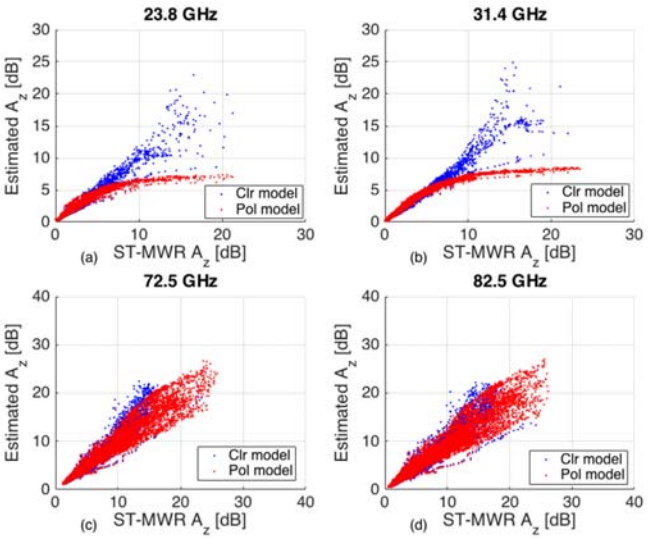

Fig. 11. Scatterplot of ST-MWR path attenuation for each frequency versus path attenuation estimated from Pol. for all weather condition. Results of the Clr models are shown as a reference.

TABLE III. ESTIMATED ZENITH-EQUIVALENT ATTENUATION ERROR CONSIDERING THE ST-MWR AVAILABLE DATASET IN 2015 IN ROME, NY FOR POL AND POLDEX MODELS

	Pol		*PolDex*		*Clr-Tmr*	
f [GHz]	AvE[dB]	RMSE[dB]	AvE[dB]	RMSE[dB]	AvE[dB]	RMSE[dB]
23.8	-0.0224	0.2502	-0.0066	0.1268	-0.0271	0.1350
31.4	-0.0068	0.3526	+0.0018	0.1475	+0.0081	0.2197
72.5	-0.0212	0.3236	-0.0046	0.3832	-0.0709	0.6199
82.5	-0.1258	0.4280	-0.0680	0.3797	-0.1624	0.6166

In (30), coupled with (27), we have introduced a dual-frequency approach to path estimation retrieval. **Table IV**, similarly to Table III, quantifies the results of this reduced-channel techique in terms of RMSE and AvE. Note how path attenuation retrieval errors from *Pol2DEx* model is still relatively small; nevertheless, higher accuracy is obtained using more than 2 Ka-band channels.

TABLE IV. SAME AS TABLE III, BUT FOR THE DUAL-FREQUENCY PREDICTION MODEL

	Pol (bifreq)		*PolDex* (bifreq)		*Tmr*	
f [GHz]	AvE[dB]	RMSE[dB]	AvE[dB]	RMSE[dB]	AvE[dB]	RMSE[dB]
23.8	-0.0178	0.2425	-0.0026	0.1272	-0.0271	0.1350
31.4	0.0045	0.3516	0.0134	0.1471	+0.0081	0.2197

C. Error budget analysis

Sect. II.C has been devoted to the discussion of the theoretical error analysis of path attenuation estimates with respect to several error sources. By using previous results, obtained from the AFRL-MWR measurements, we can now evaluate in a more quantitative way the overall error budget. The latter is shown in **Table V** which summarizes the expected errors in A and at 23.8, 31.4, 72.5 and 82.5 GHz with respect to the uncertainty of the various sources.

TABLE V. ERROR EVALUATION FOR PATH ATTENUATION ESTIMATES USING AFRL-MWR MEASUREMENTS

δA with respect to $\delta\Delta T_A$			δA with respect to δT^*_{Bsun}		
f [GHz]	$\delta\Delta T_A$[K]	δA [dB]	*f* [GHz]	δT^*_{Bsun}[K]	δA [dB]
23.8	4	-0.20	23.8	0.83	0.030
31.4	5	-0.13	31.4	0.62	0.015
72.5	12	-0.13	72.5	1.49	0.011
82.5	19	-0.14	82.5	14.3	0.085

Sensitivity δA with respect to $\delta\Delta T_A$ is given by (22a); on the left side of Table V reports the attenuation uncertainties for typical $\delta\Delta T_A$ in clear air. The latter are derived from the variability of AFRL-MWR data during the *ooS* and *twS* switching. In this case δA are less than 0.2 dB at all frequencies, slightly higher at Ka band. On the right side of Table V, a the sensitivity analysis of δA is shown with respect to uncertainties δT^*_{Bsun}. The latter has been derived from the differences between Langley and meteorological estimates shown in Table V. Errors in path attenuation retrievals are less than 0.1 dB at all frequencies. Finally, we have estimated the error in assuming the horizontal homogeneity in clear sky through the analysis of the *ooS* time series at the same elevation and different azimuths. Attenuation uncertainties are estimated to be 0.017, 0.007, 0.023, and 0.027 dB for an average azimuth distance of 5°. As such, the horizontal homogeneity assumption holds.

V. CONCLUSION

Sun-tracking microwave radiometry has been introduced to estimate the atmospheric path attenuation in all-weather conditions at Ka, V and W band. A detailed theoretical framework has been proposed to describe the Sun-tracking microwave radiometric measurement modes and to evaluate the overall error budget with respect to several sources of uncertainties. This approach has clearly identified the critical assumptions behind the ST-MWR data processing such as the accurate knowledge of the antenna beamwidth, the uniformity of incident brightness temperature within the antenna beamwidth and the atmospheric stationarity within each ST system switch.

The weighted brightness temperature of the Sun T^*_{Bsun} has been estimated by means of two different techniques, based on the elevation-scanning Langley method and the surface meteorological data method. These two techniques show comparable results, but the first one needs a careful selection of candidate clear-air days whereas the second one is depending on the external weather station data and daily variability of clear air extinction. The ST-MWR methodology has been applied to AFRL available radiometric measurements at Ka, V and W band in Rome (NY, USA) during 2015, in order to test two new physically-based prediction models for path attenuation estimation. The single-frequency double-exponential parametric model seems to outperform the multi-frequency polynomial model when compared to ST-MWR

This article has been accepted for publication in a future issue of this journal, but has not been fully edited. Content may change prior to final publication. Citation information: DOI 10.1109/TAP.2016.2606568, IEEE Transactions on Antennas and Propagation

retrievals. The clear-air based approach to estimate path attenuation, as expected, is unsuitable to estimate path attenuation in heavy cloudy and rainy conditions and at higher millimeter-wave frequency.

These results show an appealing potential of ST-MWR technique, which can be exploited to overcome the overall costs and the logistic difficulty to accomplish satellite-to-Earth radiopropagation experiments in the unexplored millimeter-wave and submillimeter-wave frequency region. A further validation of the ST-MWR technique should foresee by enlarging the available dataset and by comparing with collocated measurements performed by a satellite beacon receiver, even though the telecommunication bandwidths are typically different from the available MWR ones. The deployment of several AFRL MWRs, where PPM are applied to estimate path attenuation after a verification through ST-MWR, might allow very promising site diversity experiments at V and W band.

APPENDIX. PARAMETRIC PREDICTION MODELS

This appendix provides the tables of the regression coefficients and modeling functions used to express the physically-based parametric models (PPMs), discussed in sect. III.B. Two vPPM ersions are considered: i) multifrequency, assuming to have a disposal all 4 AFRL-MWR channels (sect. A); ii) dual-frequency, assuming to have only Ka band channels at 23.8 and 31.4 GHz (sect. B).

A. Multifrequency PPM model

Table A1 provides the regression coefficients expressions to apply *Pol* model in (26), whereas **Table A2** the same but for the *DEx* model in (27b) for each considered frequency *f* at 23.8, 31.4, 72.5 and 82.5 GHz. **Table A3** provides the Pol and PolDEx model intercomparison in terms of error indexes.

TABLE A1. PPM POLYNOMIAL MODEL COEFFICIENTS IN (26)

23.8 GHz
$a_1 = +2.51 \cdot 10^{-2} - 1.42 \cdot 10^{-2} \cdot m + 2.31 \cdot 10^{-3} \cdot m^2$
$a_2 = +8.16 \cdot 10^{-3} - 4.12 \cdot 10^{-3} \cdot m + 5.03 \cdot 10^{-5} \cdot m^2$
$a_3 = -4.18 \cdot 10^{-3} + 2.97 \cdot 10^{-3} \cdot m - 3.61 \cdot 10^{-4} \cdot m^2$
$a_4 = +1.84 \cdot 10^{-3} - 1.65 \cdot 10^{-3} \cdot m + 5.81 \cdot 10^{-4} \cdot m^2$
$b_1 = +6.04 \cdot 10^{-5} - 3.19 \cdot 10^{-5} \cdot m + 6.32 \cdot 10^{-6} \cdot m^2$
$b_2 = -2.04 \cdot 10^{-5} + 2.46 \cdot 10^{-5} \cdot m - 3.07 \cdot 10^{-6} \cdot m^2$
$b_3 = +2.67 \cdot 10^{-5} - 2.34 \cdot 10^{-5} \cdot m + 3.60 \cdot 10^{-6} \cdot m^2$
$b_4 = -1.95 \cdot 10^{-5} + 1.60 \cdot 10^{-5} \cdot m - 3.04 \cdot 10^{-6} \cdot m^2$
31.4 GHz
$a_1 = -3.37 \cdot 10^{-3} + 1.99 \cdot 10^{-3} \cdot m - 4.59 \cdot 10^{-4} \cdot m^2$
$a_2 = +4.04 \cdot 10^{-2} - 2.03 \cdot 10^{-2} \cdot m + 2.03 \cdot 10^{-3} \cdot m^2$
$a_3 = -6.13 \cdot 10^{-3} + 4.07 \cdot 10^{-3} \cdot m - 4.27 \cdot 10^{-5} \cdot m^2$
$a_4 = +9.42 \cdot 10^{-4} - 1.03 \cdot 10^{-3} \cdot m + 6.19 \cdot 10^{-4} \cdot m^2$
$b_1 = +1.60 \cdot 10^{-5} - 1.71 \cdot 10^{-5} \cdot m + 4.11 \cdot 10^{-6} \cdot m^2$
$b_2 = +2.84 \cdot 10^{-5} + 1.24 \cdot 10^{-5} \cdot m + 1.55 \cdot 10^{-7} \cdot m^2$
$b_3 = +5.53 \cdot 10^{-5} - 5.71 \cdot 10^{-5} \cdot m + 7.54 \cdot 10^{-6} \cdot m^2$
$b_4 = -3.81 \cdot 10^{-5} + 3.62 \cdot 10^{-5} \cdot m - 5.94 \cdot 10^{-6} \cdot m^2$
72.5 GHz
$a_1 = +3.37 \cdot 10^{-3} - 5.86 \cdot 10^{-3} \cdot m + 9.66 \cdot 10^{-4} \cdot m^2$
$a_2 = +2.94 \cdot 10^{-2} - 4.11 \cdot 10^{-2} \cdot m + 7.13 \cdot 10^{-3} \cdot m^2$
$a_3 = +2.75 \cdot 10^{-2} - 1.91 \cdot 10^{-2} \cdot m + 3.26 \cdot 10^{-3} \cdot m^2$
$a_4 = -1.76 \cdot 10^{-2} + 2.01 \cdot 10^{-2} \cdot m - 3.33 \cdot 10^{-3} \cdot m^2$
$b_1 = -7.61 \cdot 10^{-5} + 6.42 \cdot 10^{-5} \cdot m - 1.11 \cdot 10^{-5} \cdot m^2$
$b_2 = +4.00 \cdot 10^{-4} - 8.52 \cdot 10^{-5} \cdot m + 1.48 \cdot 10^{-5} \cdot m^2$
$b_3 = +2.51 \cdot 10^{-4} - 1.29 \cdot 10^{-4} \cdot m + 2.25 \cdot 10^{-5} \cdot m^2$
$b_4 = -1.17 \cdot 10^{-4} + 4.11 \cdot 10^{-5} \cdot m - 7.44 \cdot 10^{-6} \cdot m^2$
82.5 GHz
$a_1 = +9.71 \cdot 10^{-3} - 7.15 \cdot 10^{-3} \cdot m + 1.18 \cdot 10^{-3} \cdot m^2$
$a_2 = +4.10 \cdot 10^{-2} - 5.28 \cdot 10^{-2} \cdot m + 9.06 \cdot 10^{-3} \cdot m^2$
$a_3 = -1.19 \cdot 10^{-2} + 9.29 \cdot 10^{-3} \cdot m - 1.65 \cdot 10^{-3} \cdot m^2$
$a_4 = +1.40 \cdot 10^{-2} - 2.71 \cdot 10^{-3} \cdot m + 6.23 \cdot 10^{-4} \cdot m^2$
$b_1 = -1.60 \cdot 10^{-4} + 1.13 \cdot 10^{-4} \cdot m - 1.95 \cdot 10^{-5} \cdot m^2$
$b_2 = +4.16 \cdot 10^{-4} - 7.08 \cdot 10^{-5} \cdot m + 1.23 \cdot 10^{-5} \cdot m^2$
$b_3 = +2.05 \cdot 10^{-4} - 1.40 \cdot 10^{-4} \cdot m + 2.47 \cdot 10^{-5} \cdot m^2$
$b_4 = -4.81 \cdot 10^{-5} + 3.25 \cdot 10^{-5} \cdot m - 6.09 \cdot 10^{-6} \cdot m^2$

TABLE A2. PPM DOUBLE EXPONENTIAL MODEL COEFFICIENTS IN (27A)

23.8 GHz
$a = +1.26 - 9.27 \cdot 10^{-1} \cdot m + 1.78 \cdot 10^{-1} \cdot m^2$
$b = +6.85 \cdot 10^{-3} + 7.61 \cdot 10^{-3} \cdot m - 2.00 \cdot 10^{-3} \cdot m^2$
$c = +2.18 \cdot 10^{-14} + 2.92 \cdot 10^{-30} \cdot m - 2.70 \cdot 10^{-30} \cdot m^2$
$d = +1.17 \cdot 10^{-1} + 0.00 \cdot m - 1.42 \cdot 10^{-17} \cdot m^2$
$h = -2.01 \cdot 10^{-1} + 6.18 \cdot 10^{-1} \cdot m - 1.44 \cdot 10^{-1} \cdot m^2$
31.4 GHz
$a = +1.01 - 5.38 \cdot 10^{-1} \cdot m + 7.38 \cdot 10^{-2} \cdot m^2$
$b = +1.57 \cdot 10^{-2} - 4.56 \cdot 10^{-3} \cdot m + 1.83 \cdot 10^{-3} \cdot m^2$
$c = -9.36 \cdot 10^{-14} + 1.57 \cdot 10^{-13} \cdot m - 4.17 \cdot 10^{-14} \cdot m^2$
$d = +1.25 \cdot 10^{-1} - 1.12 \cdot 10^{-2} \cdot m + 3.14 \cdot 10^{-3} \cdot m^2$
$h = +5.34 \cdot 10^{-1} - 1.46 \cdot 10^{-1} \cdot m + 3.26 \cdot 10^{-2} \cdot m^2$
72.5 GHz
$a = +1.75 - 1.11 \cdot m + 2.03 \cdot 10^{-1} \cdot m^2$
$b = +7.56 \cdot 10^{-3} + 2.46 \cdot 10^{-3} \cdot m - 4.31 \cdot 10^{-4} \cdot m^2$
$c = -1.85 \cdot 10^{-9} - 3.88 \cdot 10^{-25} \cdot m - 7.07 \cdot 10^{-26} \cdot m^2$
$d = +8.00 \cdot 10^{-2} - 1.30 \cdot 10^{-17} \cdot m - 9.49 \cdot 10^{-18} \cdot m^2$
$h = +1.42 - 1.08 \cdot m + 2.37 \cdot 10^{-1} \cdot m^2$
82.5 GHz
$a = +1.62 - 9.43 \cdot 10^{-1} \cdot m + 1.68 \cdot 10^{-1} \cdot m^2$
$b = +8.85 \cdot 10^{-3} + 1.06 \cdot 10^{-3} \cdot m - 1.60 \cdot 10^{-4} \cdot m^2$
$c = +3.66 \cdot 10^{-10} - 2.95 \cdot 10^{-12} \cdot m + 4.76 \cdot 10^{-13} \cdot m^2$
$d = +8.51 \cdot 10^{-2} - 1.30 \cdot 10^{-17} \cdot m - 4.75 \cdot 10^{-18} \cdot m^2$
$h = +9.06 \cdot 10^{-1} - 6.27 \cdot 10^{-1} \cdot m + 1.25 \cdot 10^{-1} \cdot m^2$

This article has been accepted for publication in a future issue of this journal, but has not been fully edited. Content may change prior to final publication. Citation information: DOI 10.1109/TAP.2016.2606568, IEEE Transactions on Antennas and Propagation

TABLE A3. PPM MODEL INTERCOMPARISON

23.8 GHz						
	Pol			PolDex		
Elev[°]	AvE[dB]	RMSE[dB]	IA	AvE[dB]	RMSE[dB]	IA
90°	-0.213	1.495	0.801	-0.050	0.507	0.986
75°	-0.216	1.557	0.798	-0.047	0.511	0.987
60°	-0.229	1.777	0.784	-0.042	0.558	0.988
45°	-0.283	2.293	0.748	-0.072	0.838	0.981
36°	-0.386	2.906	0.705	-0.176	1.398	0.958
30°	-0.527	3.569	0.662	-0.338	2.144	0.918
25°	-0.698	4.380	0.620	-0.534	2.992	0.874
20°	-0.731	5.509	0.596	-0.546	3.623	0.881
31.4 GHz						
	Pol			PolDex		
Elev[°]	AvE[dB]	RMSE[dB]	IA	AvE[dB]	RMSE[dB]	IA
90°	-0.317	2.244	0.608	-0.156	1.069	0.950
75°	-0.324	2.336	0.601	-0.153	1.100	0.950
60°	-0.354	2.657	0.576	-0.150	1.222	0.951
45°	-0.443	3.394	0.511	-0.167	1.556	0.946
36°	-0.580	4.257	0.435	-0.223	1.965	0.940
30°	-0.757	5.182	0.361	-0.300	2.344	0.938
25°	-0.976	6.318	0.288	-0.376	2.708	0.943
20°	-1.096	7.940	0.237	-0.561	4.842	0.845
72.5 GHz						
	Pol			PolDex		
Elev[°]	AvE[dB]	RMSE[dB]	IA	AvE[dB]	RMSE[dB]	IA
90°	-0.391	2.892	0.834	-0.468	2.694	0.863
75°	-0.392	3.037	0.828	-0.454	2.798	0.861
60°	-0.416	3.554	0.803	-0.421	3.164	0.856
45°	-0.582	4.802	0.739	-0.441	4.020	0.843
36°	-0.953	6.331	0.660	-0.623	5.062	0.825
30°	-1.494	8.018	0.580	-0.957	6.252	0.805
25°	-2.176	10.084	0.503	-1.405	7.807	0.778
20°	-2.383	12.780	0.454	-1.383	10.154	0.742
82.5 GHz						
	Pol			PolDex		
Elev[°]	AvE[dB]	RMSE[dB]	IA	AvE[dB]	RMSE[dB]	IA
90°	-0.404	2.988	0.829	-0.458	2.903	0.838
75°	-0.407	3.135	0.822	-0.451	3.021	0.836
60°	-0.436	3.655	0.799	-0.437	3.441	0.826
45°	-0.602	4.901	0.739	-0.490	4.438	0.801
36°	-0.958	6.417	0.664	-0.688	5.641	0.771
30°	-1.481	8.083	0.590	-1.013	6.959	0.742
25°	-2.162	10.121	0.519	-1.430	8.591	0.714
20°	-2.501	12.813	0.482	-1.419	10.860	0.700

B. *Dual-frequency PPM*

Table A4 provides the regression coefficients expressions to apply *Pol2* model in (30).

TABLE A4. DUAL-FREQUENCY POLYNOMIAL MODEL COEFFICIENTS

23.8 GHz
$a_1 = +2.02 \cdot 10^{-3} - 1.14 \cdot 10^{-2} \cdot m + 2.02 \cdot 10^{-3} \cdot m^2$
$a_2 = +3.86 \cdot 10^{-3} - 2.82 \cdot 10^{-3} \cdot m + 3.09 \cdot 10^{-4} \cdot m^2$
$b_1 = +9.62 \cdot 10^{-5} - 6.71 \cdot 10^{-5} \cdot m + 1.28 \cdot 10^{-5} \cdot m^2$
$b_2 = -1.04 \cdot 10^{-5} + 2.12 \cdot 10^{-5} \cdot m - 3.65 \cdot 10^{-6} \cdot m^2$
31.4 GHz
$a_1 = -6.19 \cdot 10^{-3} + 5.84 \cdot 10^{-3} \cdot m - 8.77 \cdot 10^{-4} \cdot m^2$
$a_2 = +3.19 \cdot 10^{-2} - 2.02 \cdot 10^{-2} \cdot m + 3.23 \cdot 10^{-3} \cdot m^2$
$b_1 = +3.45 \cdot 10^{-5} - 4.32 \cdot 10^{-5} \cdot m + 8.55 \cdot 10^{-6} \cdot m^2$
$b_2 = +7.25 \cdot 10^{-5} - 1.26 \cdot 10^{-5} \cdot m + 2.36 \cdot 10^{-6} \cdot m^2$

ACKNOWLEDGMENT

The contribution of A.V. Bosisio (CNR, Italy) P. Ciotti (Univ. of L'Aquila) and P. Basili (Univ. of Perugia) for data analysis is acknowledged. The work of L. Milani was carried out within the Excellence program of the Sapienza University of Rome.

REFERENCES

[1] L. J. Ippolito, "Radio propagation for communications", *IEEE Proc.*, vol. 69, pp. 697-727, 1981.

[2] G. Maral, M. Bousquet, and Z. Sun (Contributing Editor), Satellite Communications Systems: Systems, Techniques and Technology, 5th Edition, ISBN: 978-0-470-71458-4, 742 pages, Wiley (Hoboken, NJ, USA) Dec. 2009.

[3] G. Brussaard and P. A.Watson, *Atmospheric Modelling and Millimetre Wave Propagation*. London, U.K.: Chapman & Hall, 1995.

[4] B. R. Arbesser-Rastburg and A. Paraboni, "European research on Ka-band slant path propagation," Proc. IEEE, vol. 85, no. 6, pp. 843–852, Jun. 1997.

[5] R. Polonio and C. Riva, "ITALSAT propagation experiment at 18.7, 39.6, and 49.5 GHz at Spino d'Adda: Three years of CPA statistics," IEEE Trans. Antennas Propagat., vol. 46, no. 5, pp. 631–635, May 1998.

[6] X. Boulanger, Gabard, B.; Casadebaig, L.; Castanet, L., "Four Years of Total Attenuation Statistics of Earth-Space Propagation Experiments at Ka-Band in Toulouse," IEEE Transactions on Antennas and Propagation, vol. 63, pp. 2203-2214, doi: 10.1109/TAP.2015.2407376, May 2015.

[7] C. Riva, L. Castanet, L. Csurgai-Horvath, O. Fiser, F. Lacoste, F.S. Marzano, F. Perez Fontan, J.M. Riera, A. Rocha, M. Schönhuber, A. Vilhar, "The Aldo Paraboni Scientific Experiment: The Preparation And Plans For An European Measurement Campaign", Proc. of Joint 20th Ka and Broadband Communications, Navigation and Earth Observation Conference, Salerno/Vietri (Italy), 1-3 Oct. 2014.

[8] M. Montopoli and F.S. Marzano, "Maximum likelihood retrieval of modeled raincell patterns from mid-latitude C.band weather radar", IEEE Trans. Geosci. Rem. Sensing, ISSN: 0196-2892, vol. 45, n. 7, pp. 2403-2416, 2007.

[9] F.S. Marzano, "Predicting antenna noise temperature due to rain clouds at microwave and millimeter-wave frequencies", IEEE Trans. Antennas and Propagat., ISSN: 0018-926X, vol. 55, n. 7, pp. 2022-2031, 2007.

[10] C. Capsoni, M. D'Amico, and T. Tarsi, "Statistical Characterization of Path Attenuation of Radar Signals at C Band", Journal of Atmospheric and Oceanic Technology, Vol. 18, No. 4, pp. 609- 615, 2001.

[11] A. Ishimaru and R. L.-T. Cheung, "Multiple-scattering effect on radiometric determination of rain attenuation at millimeter-wavelengths," Radio Sci., vol. 15, pp. 507–516, 1980

[12] F. S.Marzano, E. Fionda, and P. Ciotti, "Simulation of radiometric and attenuation measurements along earth-satellite links in the 10- to 50-GHz band through horizontally-finite convective raincells," Radio Sci., vol. 34, pp. 841–858, 1999.

[13] F.S. Marzano, E. Fionda, and P. Ciotti, "A neural network approach to precipitation intensity and extinction retrieval by ground-based passive microwave technique", J. Hydrology, ISSN: 0022-1694, DOI: 10.1016/j.hydrol.2005.11.42, vol. 328, pp. 121-131, 2006

[14] F.S. Marzano, "Modeling antenna noise temperature due to rain clouds at microwave and millimeter-wave frequencies", IEEE Trans. Antennas and Propagat., ISSN: 0018-926X, vol. 54, pp. 1305-1317, 2006.

[15] J. Güldner, "A model-based approach to adjust microwave observations for operational applications: results of a campaign at Munich Airport in winter 2011/2012," *Atmos. Meas. Tech.*, 6, 2879–2891, 2013,www.atmos-meas-tech.net/6/2879/2013/.doi:10.5194/amt-6-2879-2013.

[16] V. Mattioli, F. S. Marzano, N. Pierdicca, C. Capsoni, and A. Martellucci, "Sky-Noise Temperature Modelling and Prediction for Deep Space Applications from X Band To W Band" IEEE Trans. of Antennas and Propagation, Volume: 61 , Issue: 7 Page(s): 3859 – 3868, 2013

[17] G. Brost, K. Magde, and W. Cook, "Radiometer Based measurements of Slant-Path Attenuation in the V/W bands", *Proc. of 13th Specialist Meeting on Microwave Radiometry and Remote Sensing of the Environment* (MicroRad), Pasadena (CA), pp. 118-123, 2014

[18] R.J. Coates, "Measurements of Solar Radiation and Atmospheric Attenuation at 4.3-Millimeters Wavelength", *Proc. of the IRE*, pp. 122-126, Jan. 1958.

[19] F. I. Shimabukuro and J. M. Stacey, "Brightness temperature of the quiet Sun at centimetre and millimetre wavelengths", The Astrophysical Journal, Vol 152, June 1968.

This article has been accepted for publication in a future issue of this journal, but has not been fully edited. Content may change prior to final publication. Citation information: DOI 10.1109/TAP.2016.2606568, IEEE Transactions on Antennas and Propagation

[20] M.M. Franco, S.D. Slobin, C.T. Stelzried, "20.7 and 31.4-GHz Solar Disk Temperature measurements", TDA progress Report 42-64, pp. 140-168, 1981.

[21] D.C. Hogg and Ta-Shing Chu, "The role of rain in satellite communications," in Proceedings of the IEEE, vol. 63, no.9, pp.1308-1331, Sept. 1975, doi 10.1109/PROC.1975.9940.

[22] D.L. Croom, "Sun as a broadband source for tropospheric attenuation measurements at millimetre wavelengths," in Electrical Engineers, Proceedings of the Institution of, vol. 120, no.10, pp.1200-1206, October 1973, doi: 10.1049/piee.1973.0244.

[23] K. Shimada, M. Higashiguchi, and Y. Otsu, "Characteristics of Atmospheric Attenuation at 35 GHz Obtained by Sun Track Measurements", Electronics and Communications in Japan, vol. 67-B, No 2, pp. 26-36, 1984.

[24] V. Mattioli, F.S. Marzano, P. Basili, P. Ciotti, A.V. Bosisio, K. Magde, G. Brost, Modeling and prediction of tropospheric radiopropagation parameters from ground-based multi-channel radiometric measurements between Ka and W band, Proceedings of 9th European Conference on Antennas and Propagation (EuCAP), pp. 1– , 2015.

[25] V. Mattioli, F.S. Marzano, N. Pierdicca, G. Brost, P. Basili, P. Ciotti, Modeling radio propagation effects at V- and W-band using physical-statistical approaches and ground-based data, Proceedings of 7th European Conference on Antennas and Propagation (EuCAP), pp. 2287 – 2291, 2013.

[26] T. Rose, ESA ATPROP System (RPG-HATPRO & RPG-15-90), Version 2.00, Radiometer Physics GmbH (www.radiometer-physics.com), pp. 190, 2008.

[27] F.T. Ulaby, R.K.Moore and A.K.Fung, *Microwave Remote Sensing Active and Passive*, Vol.1, Addison-Wesley, 288-302, 1981.

[28] S. M. Adler-Golden and J. R. Slusser, "Comparison of Plotting Methods for Solar Radiometer Calibration", J. Atmos. Oceanic Technol., vol. 24, pp. 935–938, 2007

[29] F.S. Marzano and C. Riva, "Cloud-induced effects on long-term amplitude scintillation along millimeter-wave slant paths", IEEE Trans. Antennas Propagat., ISSN: 0018-926X, vol. 51, n. 4, pp. 880-887, 2003

[30] V. Mattioli, A. Graziani, P. Tortora, A.V. Bosisio, L. Castanet, "Analysis and improvements of methodologies for discriminating atmospheric conditions from radiometric brightness temperatures" Proc. of the 7th European Conference on Antennas and Propagation (EuCAP), pp. 1392 – 1396, 2013.

[31] A.V. Bosisio, G. Graziani, V. Mattioli, P. Tortora, "On the Use of Microwave Radiometers for Deep Space Mission Applications by Means of a Radiometric-Based Scalar Indicator", IEEE Journal of Selected Topics in Applied Earth Observations and Remote Sensing, vol. 8 issue 9, pp. 4336-4344, 2015.

[32] V. Mattioli, P. Basili, S. Bonafoni, P. Ciotti, E. R. Westwater, "Analysis and improvements of cloud models for propagation studies", Radio Sci., 44, RS2005, Mar 2009, doi:10.1029/2008RS003876.

[33] J. A. Schroeder, and E. R. Westwater, Users' guide to WPL microwave radiative transfer software, *NOAA Tech. Rpt. ERL-219 WPL-213*, 84 pp., NOAA/Environmental Research Laboratories, Boulder ,CO, 1991.

[34] P.W. Rosenkranz, Correction to water vapor microwave continuum absorption: a comparison of measurements and models, *Radio Sci.*, vol. 34, n. 4, pp. 1025, 1999.

[35] C.J. Willmott, S.M. Robesonb and K. Matsuuraa, "A refined index of model performance," Int. J. Climatol. vol. 32, pp. 2088–2094, 2012.

Frank S. Marzano (S'89–M'99–SM'03-F'16) received the Laurea degree (*cum laude*) in Electrical Engineering (1988) and the Ph.D. degree (1993) in Applied Electromagnetics both from the University of Rome "La Sapienza", Italy. In 1992 he was a visiting scientist at Florida State University, Tallahassee, FL. During 1993 he collaborated with the Institute of Atmospheric Physics, National Council of Research (CNR), Rome, Italy. From 1994 till 1996, he was with the Italian Space Agency, Rome, Italy, as a post-doctorate researcher. After being a lecturer at the University of Perugia, Italy, in 1997 he joined the Department of Electrical Engineering, University of L'Aquila, Italy teaching courses on electromagnetic fields as Assistant Professor. In 1999 he was at Naval Research Laboratory, Monterey, CA, as a visiting scientist. In 2002 he got the qualification to Associate Professorship and has co-founded Center of Excellence on Remote Sensing and Hydro-Meteorological Modeling (CETEMPS), L'Aquila. In 2005 he finally joined the Dept. of Information engineering, Electronics and Telecommunications, Sapienza Univ. of Rome, Italy where he presently teaches courses on antennas, propagation and remote sensing. Since 2007 he is vice-director of CETEMPS of the University of L'Aquila, Italy where he became Director in 2013. His current research concerns passive and active remote sensing of the atmosphere from ground-based, airborne, and space-borne platforms and electromagnetic propagation studies. Dr. Marzano has published more than 130 papers on refereed International Journals, more than 30 contributions to international Book chapters and more than 300 extended abstract on international and national congress proceedings. He was the Editor of 2 books. Since January 2004 he has been acting as an *Associated Editor* of IEEE Geoscience Remote Sensing Letters. In 2005 and 2007 he has been Guest Co-Editor of the MicroRad04 and MicroRad06 Special Issues for IEEE-GRSL. Since January 2011 he is Associate Editor of the journal EGU Atmospheric Measurements Techniques. He is a Fellow of IEEE and UK Royal Meteorological Society as well as member of the MWI-ICI Science Advisory Group of EUMETSAT and GPM Science Team of NASA.

Vinia Mattioli (M'03) received the M.S. degree in electronic engineering and the Ph.D. degree from the University of Perugia, Perugia, Italy, in 2001 and 2005, respectively. From 2005 to 2012, she was with the Department of Electronic and Information Engineering, Perugia, Italy, and with the Department of Information Engineering, Electronics and Telecommunications, Sapienza University of Rome, Italy, as a postdoctoral research associate. Since 2013 she is with EUMETSAT in Darmstadt, Germany, as a calibration consultant for EPS-SG MWI and ICI spaceborne radiometers. Between 2003 and 2004, she received a Ph.D. scholarship to conduct research at the Environmental Technology Laboratory, NOAA, Boulder, CO, and between 2011 and 2012, she was visiting scientist at the Electromagnetics and Radar Department at Onera, Toulouse, France. She was part of the Management Committee of the COST Action IC0802, on propagation tools and data for integrated telecommunication, navigation and Earth Observation Systems. Her research interests included radiometer calibration techniques, passive ground-based and satellite-based microwave atmospheric remote sensing, physical and statistical modeling for radio propagation applications, microwave radiative transfer models and GPS applied to remote sensing.

Luca Milani (M'16) received the B.Sc. degree (*cum laude*) in electronic engineering and the M.Sc. degree (*cum laude*) in electronic engineering from the University of Rome "La Sapienza", Italy, in 2013 and 2015, respectively. In 2015-16 he worked at ESA/ESOC in Darmstadt (Germany) for 5 months on deep space communication links and data processing. In 2016 he joined the Department of Information Engineering (DIET), University of Rome "La Sapienza", Italy, to cooperate on research activities about ground-based and space-based microwave radiometry and atmospheric radiopropagation at Ka band and above.

Kevin M. Magde received the B. Sc. degree in computer engineering from the Rochester Institute of Technology in 1987 and the M. Sc. degree in electrical engineering from Syracuse University in 1994. He has worked on in-house projects for the USAF since 1985. The period from 1985 to 2005 consisted of research in the field of optics, and during 2005 to 2010 work on radar signal processing was performed. Currently he works in a group concerned with using radiometers to measure attenuation statistics in the V/W-band.

George A. Brost received the Ph.D. degree in physics from Washington State University in 1984. From 1984 to 1988 he was a NRC Post Doctorate Fellow and visiting scientist at F. J. Seiler Research Lab, USAF Academy. Since 1988 he has been with the Air Force Research Laboratory in Rome NY. His research has encompassed a broad range of activities involving the propagation and interaction of electromagnetic waves with matter. His is currently involved in the development of advanced satellite communications technology with a focus on propagation and atmospheric effects on millimeter waves.

This article has been accepted for publication in a future issue of this journal, but has not been fully edited. Content may change prior to final publication. Citation information: DOI 10.1109/TAP.2016.2606568, IEEE Transactions on Antennas and Propagation

List of figures

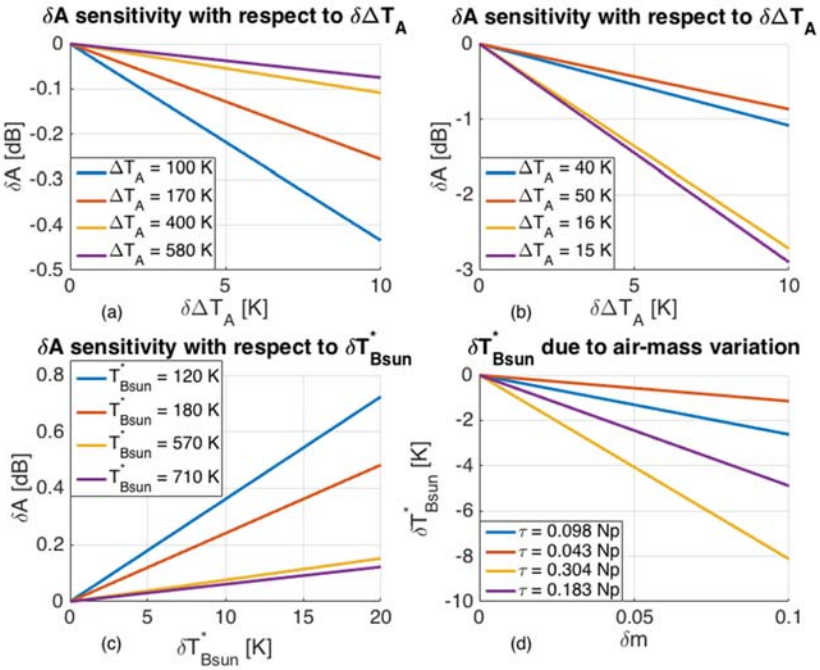

Fig. 1. Sensitivity analysis of ST-MWR performances for a set of T^*_{Bsun} values which are those expected between Ka and W band. Blue line corresponds to 23.8 GHz, red line to 31.4 GHz, yellow line to 72.5 GHz and finally violet line to 82.5 GHz. See text for details.

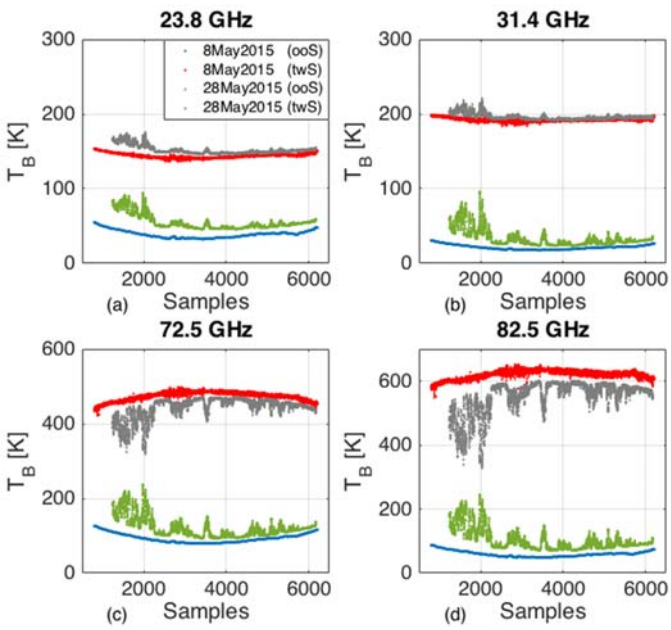

Fig. 2. Time series of ST-MWR measurements in terms of *ooS* (lower couple of curves) and *twS* (upper couple of curves) antenna noise temperatures for two case studies referring to a clear air (8 May 2015, blue dots for *ooS* and red dots for *twS*) and cloudy day (28 May 2015, green dots for *ooS* and grey dots for *twS*) and for the AFRL-MWR available frequencies a) 23.8 GHz; b) 31.4 GHz; c) 72.5 GHz; d) 82.5 GHz.

This article has been accepted for publication in a future issue of this journal, but has not been fully edited. Content may change prior to final publication. Citation information: DOI 10.1109/TAP.2016.2606568, IEEE Transactions on Antennas and Propagation

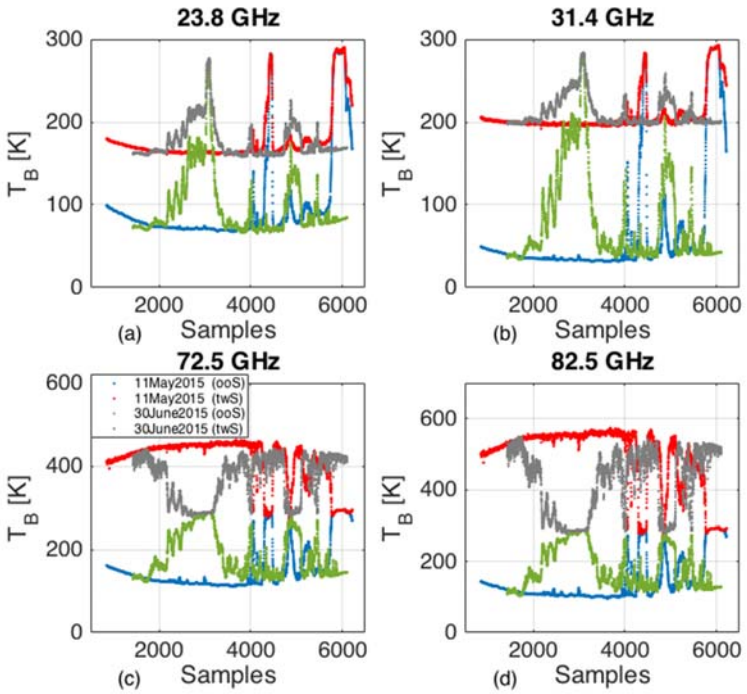

Fig. 3. Time series of ST-MWR measurements as in Fig. 2, but for two case studies referring to a moderate rain (11 May 2015, blue dots for *ooS* and red dots for *twS*) and intense rain event (30 June 2015, green dots for *ooS* and grey dots for *twS*) for the four AFRL-MWR available frequencies a)-d).

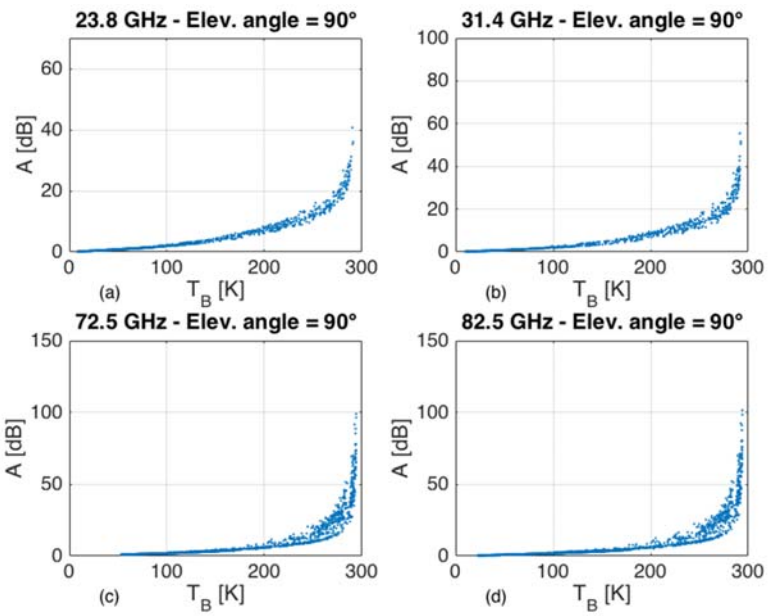

Fig. 4. Scatterplot of T_{BooS} versus corresponding path attenuation A at zenith (elevation angle of 90°) in all weather conditions for each considered frequency a) 23.8 GHz; b) 31.4 Ghz; c) 72.5 GHz; d) 82.5 GHz.

This article has been accepted for publication in a future issue of this journal, but has not been fully edited. Content may change prior to final publication. Citation information: DOI 10.1109/TAP.2016.2606568, IEEE Transactions on Antennas and Propagation

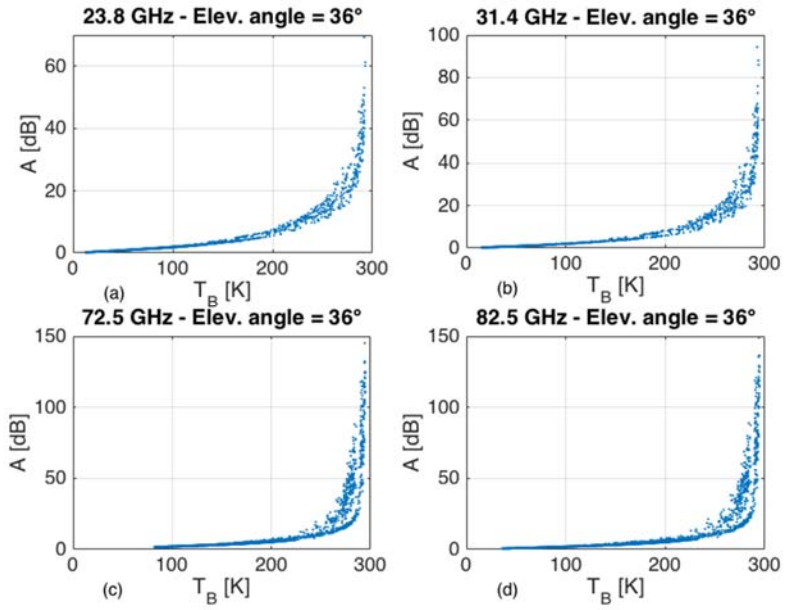

Fig. 5. The same as in Fig. 4, but for an elevation angle of 36°.

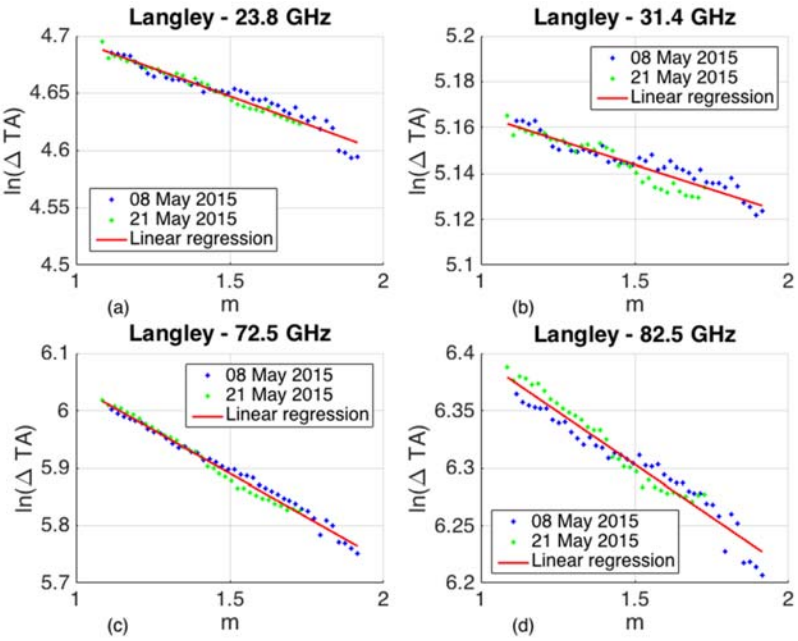

Fig. 6. Estimate of T^*_{Bsun} using the Langley technique, as discussed in sect. II.B, for each frequency and the 2 selected clear-air days.

This article has been accepted for publication in a future issue of this journal, but has not been fully edited. Content may change prior to final publication. Citation information: DOI 10.1109/TAP.2016.2606568, IEEE Transactions on Antennas and Propagation

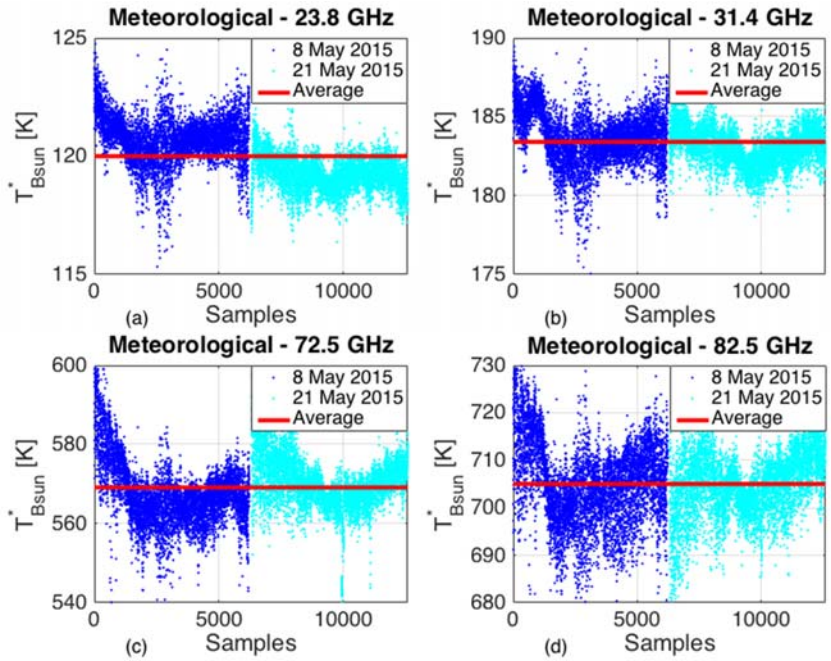

Fig. 7. Estimate of T^*_{Bsun} using the meteorological technique for the two selected clear-sky days (May 8, blue dots; May 21 cyan dots) at each frequency a) 23.8 GHz; b) 31.4 GHz; c) 72.5 GHz; d) 82.5 GHz.

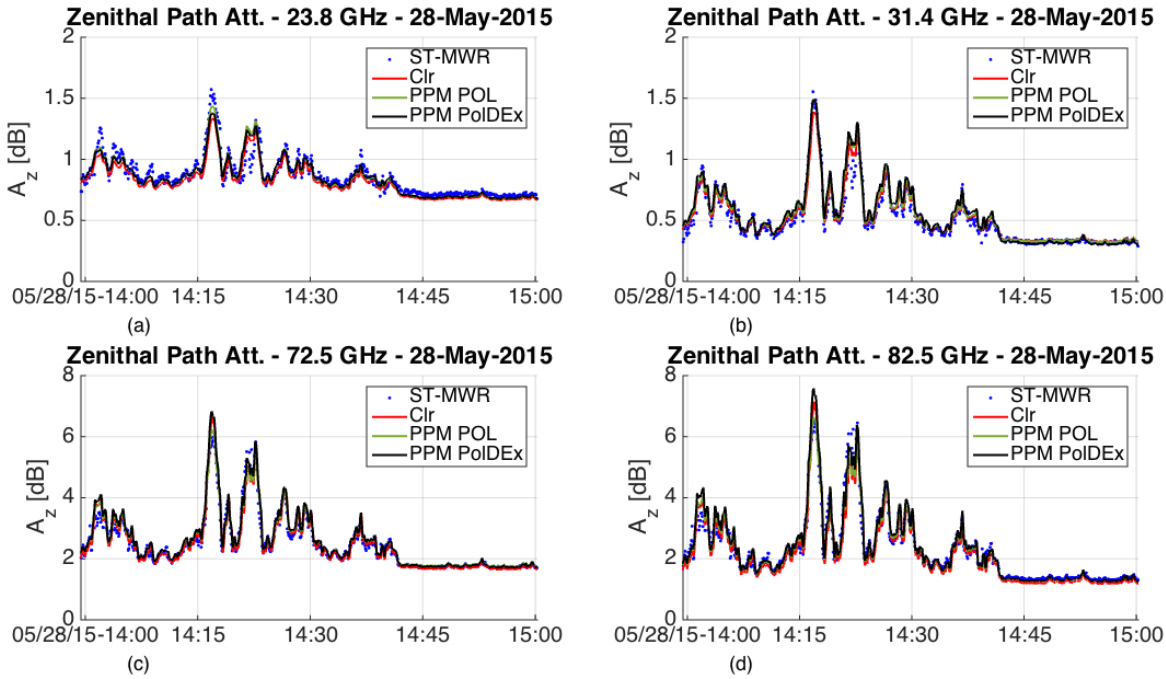

Fig. 8. Time series of zenith-equivalent path attenuation estimates on May 28, 2015 (cloudy case) at a) 23.8 GHz; b) 31.4 GHz; c) 72.5 GHz; d) 82.5 GHz.

This article has been accepted for publication in a future issue of this journal, but has not been fully edited. Content may change prior to final publication. Citation information: DOI 10.1109/TAP.2016.2606568, IEEE Transactions on Antennas and Propagation

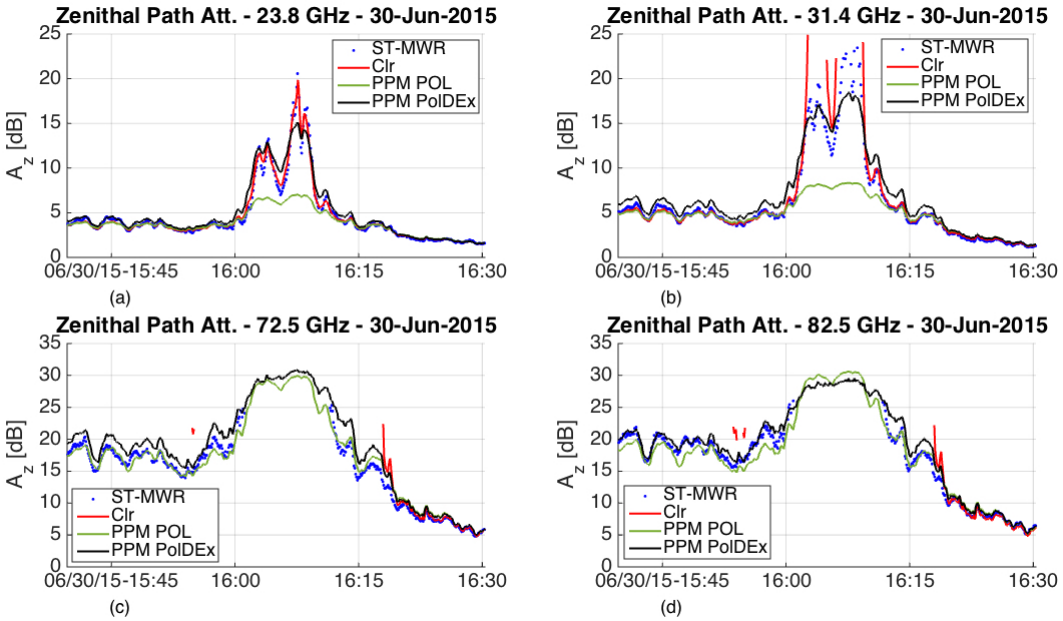

Fig. 9. Time series of zenith-equivalent path attenuation estimates on June 30, 2015 (rainy event) at a) 23.8 GHz; b) 31.4 GHz; c) 72.5 GHz; d) 82.5 GHz.

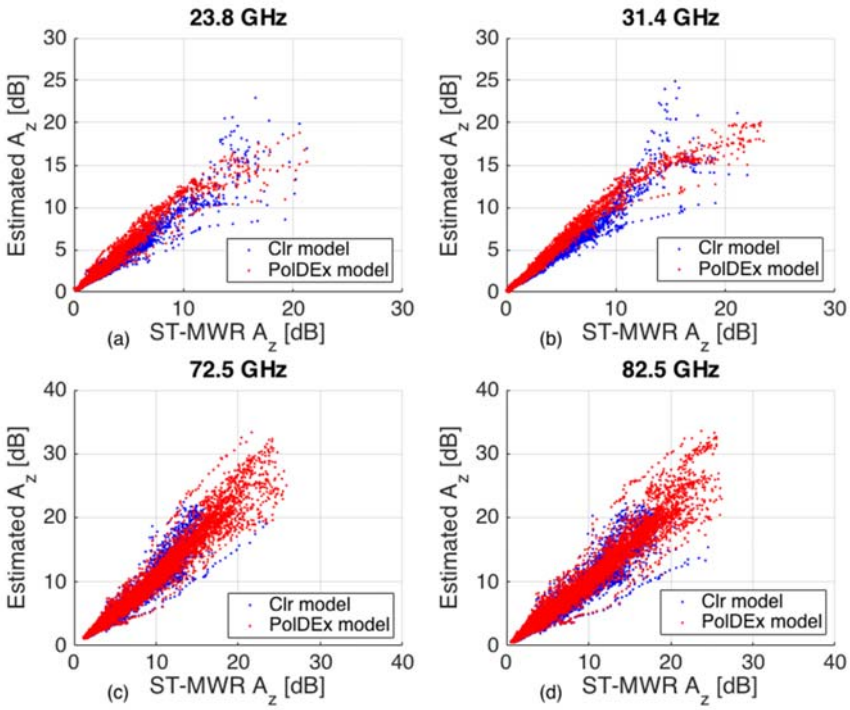

Fig. 10. Scatterplot of ST-MWR path attenuation for each frequency versus path attenuation estimated from PolDEx and Clr models for all weather condition.

This article has been accepted for publication in a future issue of this journal, but has not been fully edited. Content may change prior to final publication. Citation information: DOI 10.1109/TAP.2016.2606568, IEEE Transactions on Antennas and Propagation

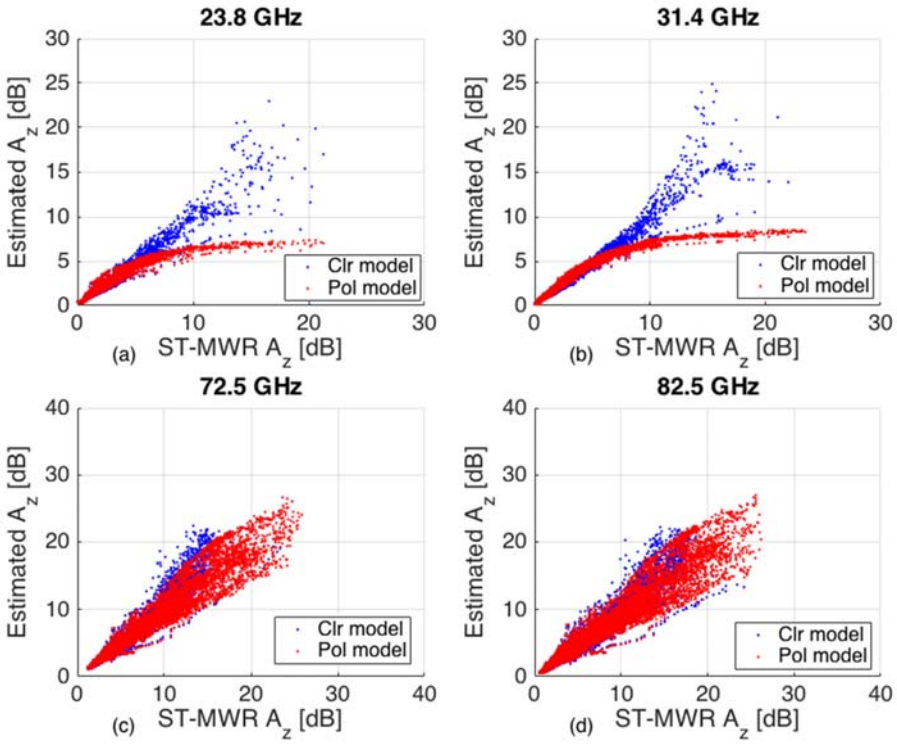

Fig. 11. Scatterplot of ST-MWR path attenuation for each frequency versus path attenuation estimated from Pol. for all weather condition. Results of the Clr models are shown as a reference.